Exploring the Accuracy of RANS Simulations for Mars Entry Vehicles

Clark C. Pederson*, Mark Schoenenberger†
NASA Langley Research Center, Hampton, VA, 23681, USA

Accurate yet inexpensive predictions of aerodynamic coefficients for Mars entry vehicles have remained a consistent challenge over the past five decades. Below Mach 6, drag on the backshell becomes significant and must be accurately predicted. Steady Reynolds-averaged Navier-Stokes (RANS) models are commonly used, despite their poor predictions of backshell pressure. While scale-resolving simulations have shown promise in the past decade, there is still a need for cheap, accurate RANS predictions for large aerodynamic databases. The Mars Science Laboratory (MSL) is used as a case study to examine predictive accuracy and known shortcomings for RANS predictions of Mars entry vehicles. Several different grid generation techniques are compared, including a comparison between prismatic boundary layer grids and fully unstructured, tetrahedral grids. Comparisons are made to experimental data for Mach 2.5, 3.5, and 4.5. The accuracy of predicted aerodynamic coefficients is examined. Overpredictions in axial force and drag are explained by a closer examination of the surface pressure. These findings document sensitivities and best practices for future RANS database development of Mars entry vehicles.

Nomenclature

C_A	=	Axial force coefficient
C_D	=	Drag coefficient
C_L	=	Lift coefficient
C_N	=	Normal force coefficient
C_m	=	Pitching moment
c_p	=	Pressure coefficient
D	=	Aeroshell diameter
M	=	Mach number
Re_D	=	Reynolds number based on vehicle diameter
T	=	Temperature
u	=	Velocity
x	=	Axial direction
y	=	Direction perpendicular to the symmetry plane
z	=	Direction perpendicular to the x and y axes
α	=	Angle-of-attack
β	=	Side-slip angle
Δy^+	=	Wall-normal spacing, normalized by viscous length
ρ	=	Density
μ	=	Dynamic viscosity
τ_w	=	Wall shear stress

I. Introduction

STARTING with the original Viking missions, researchers struggled to predict the aerodynamics of a Mars entry vehicle. Campbell and Brown [1] described "extreme difficulties" modeling the wake pressure for Viking landers. These

*Aerothermodynamics Branch, AIAA Member
†Aerospace Engineer, Atmospheric Flight and Entry Systems Branch, Senior Member AIAA

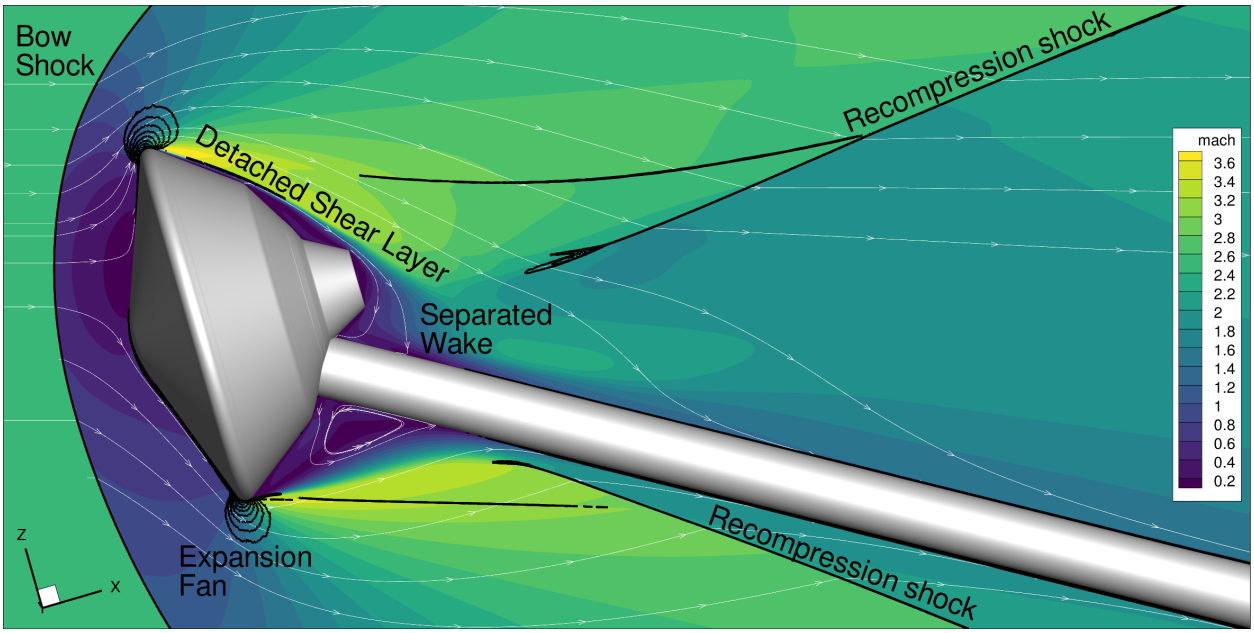

Fig. 1 Illustration of the flow features for an MSL geometry, mounted on a sting, at Mach 2.5, $Re_D = 10^6$, and $\alpha = -16°$.

difficulties in modeling the backshell have continued during recent missions, such as the Mars Science Laboratory (MSL) and Mars 2020 [2]. The most common method for database development in this speed regime is to predict steady solutions with Reynolds-averaged Navier-Stokes (RANS) models for the turbulence. RANS models only resolve the average flow, and attempt to model the whole spectrum of turbulent fluctuations. These models are relatively accurate for the attached boundary layers on the forebody of an aeroshell; the pressure can usually be predicted to within a few percent. However, these models struggle to accurately predict massively separated wakes.

As the Mach number decreases, the backshell pressure forms a larger percentage of the total axial force. This can be seen in Fig. 2, where the estimated backshell contribution to drag is shown for the Mars 2020 mission. The backshell contribution is estimated using the MEDLI2 flight data from Mars 2020 [3]. While above Mach 6 the backshell only contributes 1% or less of the drag, the contribution is as high as 17% at Mach 2. At lower speeds, modeling errors in drag can no longer be safely ignored. As new geometries are evaluated for human Mars missions and margins become smaller, there is a strong need to improve the accuracy of these aerodynamic predictions with limited computational costs.

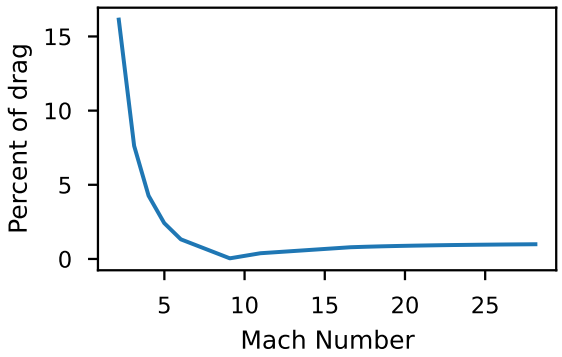

Fig. 2 Estimates for the percent contribution to axial force from the backshell, as a function of freestream Mach number. Data are from the Mars 2020 post-flight reconstruction [3]

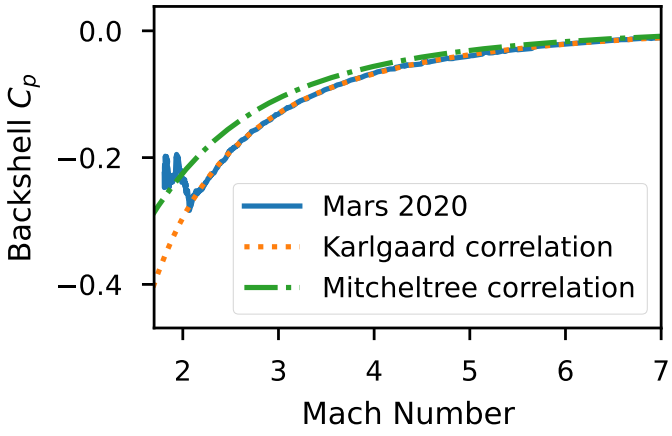

Fig. 3 MEDLI2 pressure in the separated wake for Mars 2020, as a function of Mach number. Also plotted are correlations to Viking data by Mitcheltree [11] and a correlation to the Mars 2020 data by Karlgaard et al. [3]

These difficulties are not unique to entry, descent, and landing. Various studies [4–6] have shown that even for an incompressible flow over a bluff body, steady RANS will overpredict the size of the separated wake and underpredict the drag. Compressibility changes the nature of the problem, since an expansion occurs across the detached shear layers. Forsythe et al. [7] showed that steady RANS models underpredict the base pressure of a supersonic base flow. Their study also demonstrated the importance of grid quality by comparing structured versus unstructured grids and unstructured versus prismatic boundary layers. The various meshing techniques yielded pressure differences of 20% in the wake. The study demonstrated that careful grid generation is critical for accurate aerodynamic predictions of wake flows. Later, Schwing and Candler [8] modeled an Orion reentry capsule at subsonic and supersonic Mach numbers; they reported that steady RANS consistently overpredicted drag, sometimes by as much as 18%.

These same ideas have been repeated across several Mars missions over several decades. Steady RANS models typically underpredict the wake pressure, leading to an overestimation of drag. During the post-flight analysis of Mars 2020, Ekelschot and Brock [9] found that steady RANS underpredicted wake pressures by 28% at Mach 4, and 37% at Mach 3. For the Schiaparelli entry module, Brandis et al. [10] showed a 20–40% overprediction of the backshell pressure when compared with flight data.

In the past, empirical formulas based on wind tunnel or flight data have been used for ad hoc corrections to CFD. Mitcheltree [11] developed an empirical formula to predict backshell pressure based on Viking data. This formula was used for the backshell drag on both the Mars Science Lander [2] and the Mars 2020 landers, and is included in that reference. While empirical formulas are useful for current missions, they are ad hoc in nature and have unknown accuracy when extrapolated to new vehicle geometries or new flight trajectories. This is evident when considering the flight data from the Mars 2020 mission. The Mars 2020 lander was equipped with 8 different pressure transducers, including on the wake region of the backshell. Full details can be found in Refs. [3, 12]. Karlgaard et al. [3] created an empirical correlation to the backshell pressure, which is plotted as a function of reconstructed Mach number in Fig. 3. At the lowest Mach numbers, before the entry mass jettison, the difference between the measured pressure and the Mitcheltree correlation was about $\Delta c_p = -0.10$. Given that the backshell accounted for 17% of the drag force at $M_\infty = 2$, pressure errors of ± 0.1 are unacceptably large. These differences between the Mitcheltree correlation and the Mars 2020 flight data are not surprising; the Mitcheltree correlation is based on data from the Viking lander, which had a smaller shoulder radius and smaller backshell. The Mars Sample Retrieval Lander, which is scheduled to launch in 2028, has a backshell that is much larger than previous vehicles. New geometries such as the Hypersonic Inflatable Aerodynamic Decelerator [13] will be necessary for human missions to Mars, but have radically different backshell geometries. Empirical formulas from previous missions can be descriptive, but they will not be predictive for new geometries.

Scale-resolving simulations are an alternative to steady RANS simulations. Instead of resolving only a single mean field, these simulations resolve the time-dependent behavior. Conceptually, the simplest method is large-eddy simulation (LES), where the largest scales of turbulence are directly resolved and the effects of the smallest scales are modeled.

Another common scale-resolving simulation is hybrid RANS/LES, in which regions of RANS and LES modeling are combined in a single simulation. Hybrid RANS/LES methods have repeatedly shown superior accuracy in predicting compressible, separated wakes [7, 8, 14, 15]. Scale-resolving simulations represent the state-of-art in aerodynamic predictions for Mars entry vehicles. Nevertheless, there is still a strong need for RANS because scale-resolving simulations carry a significantly higher computational cost. RANS is the tool of choice for cheaper computations and faster turnarounds, at least for the next decade (see Refs. [16, 17]). The generation of flight databases for Mars missions can require hundreds of simulations, for which scale-resolving simulations are currently infeasible. Many other applications require lower computational cost, including Monte Carlo uncertainty quantification and iterative design optimization.

Several research trends have emerged in the last three decades, which purport to improve accuracy beyond the CFD used for Pathfinder or MSL. One such area of research is grid generation. Studies such as that by Forsythe et al. [18] and Thompson et al. [19] demonstrate that compressible wakes can be very sensitive to the grid quality. Structured grids have been used for previous Mars programs, such as MSL [2, 20] and the ballistic range tests for Mars 2020 [14, 21]. However, structured grids are difficult to generate for complex geometries required by future missions [19], such as a Hypersonic Inflatable Aerodynamic Decelerator [13]. This motivates the use of unstructured grids and mesh adaptation. Several publications have already demonstrated the potential of Hessian-based anisotropic mesh adaptation for Mars entry vehicles. Kleb et al. [22] demonstrated mesh adaptation for the reaction control jets on the Mars Sample Return Lander. Ekelschott et al. [23, 24] used anisotropic mesh adaptation for their predictions of the surface pressure on the Mars 2020 vehicle. Both papers noted significant savings in grid generation time through automated solution adaptation.

There are several competing ideas for how to best apply anisotropic mesh adaptation for high-speed flows. The work by Kleb et al. [22] used an unstructured, tetrahedral grid through the whole domain, including the bow shock and boundary layer. Using a fully tetrahedral mesh greatly simplifies the mesh generation and adaptation process. Another alternative is hybrid meshes, which combine prismatic layers with regions of pure tetrahedra. These techniques were pioneered by Nakahashi [25] and Kallinderis et al. [26, 27]. McCloud [28] presented a technique for inserting a structured grid both near the body as well as around a bow shock, while leaving unstructured tetrahedra in the rest of the mesh. Nastac et al. [29] and Ekelschot and Brock [23, 24] demonstrated a similar approach by building a prismatic boundary layer, but used unstructured tetrahedra through the shocks. These hybrid meshes are preferred for several reasons. First, hybrid meshes give fine-grained control over the wall-normal spacing, since this is usually specified manually. Second, Roe-type convective flux schemes have been shown to be only first-order accurate on irregular meshes [30, 31]. Finally, a Galerkin discretization of the viscous terms is inconsistent for some irregular meshes, and results in an $O(1)$ error [32]. Because they are more regular, prismatic boundary layers help to maintain second-order accuracy and minimize the errors in a Galerkin discretization of the viscous terms. Prismatic boundary layer grids are often preferred when predicting quantities such as skin friction or heat transfer, which are sensitive to the boundary layer properties. Pressure contours are less sensitive, since the surface pressure for entry vehicles is dominated by inviscid effects and the boundary layer only plays a secondary role. The split in the literature reflects a strong need to compare the predictive accuracy on different grid types.

Several other model improvements purport to improve RANS model accuracy. For example, Brown et al. [33] improved wake flow predictions of a hypersonic wake by using compressibility corrections. This stands in contrast to the study by Forsythe et al. [7], who showed that compressibility corrections resulted in unphysical variations in pressure across the wake. Innovation continues to occur for RANS modeling, including corrections for rotation, curvature, and Reynolds-stress anisotropy. Given that steady RANS is expected to be used in some capacity until at least 2030, there is a significant need to quantify the accuracy of RANS-based approaches for Mars entry aerodynamics, as well as document the institutional knowledge learned through previous missions.

This paper will begin with a discussion of the experimental data used for validation, along with the typical quantities of interest for experiments and project requirements. The next section covers the computational tools used for the CFD. The rest of the paper is split into two separate validation exercises. The first focuses on a comparison of grid generation technique for a simple forebody-only case. The second focuses on full-body CFD using a fully tetrahedral mesh.

II. Experimental Data

This paper uses the Mars Science Laboratory as a case study for entry vehicle CFD, in part because of the amount of experimental data available. From 2007–2010, tests were carried out in the Langley Unitary Plan Wind Tunnel (LUPWT) to characterize the aerodynamics of the MSL aeroshell [2, 20, 34]. LUPWT test 1811 measured all three aerodynamic forces and three moments. LUPWT test 1855 used pressure taps to supply more fine-grained aerodynamic

(a) Schlieren image with the 30-degree sting

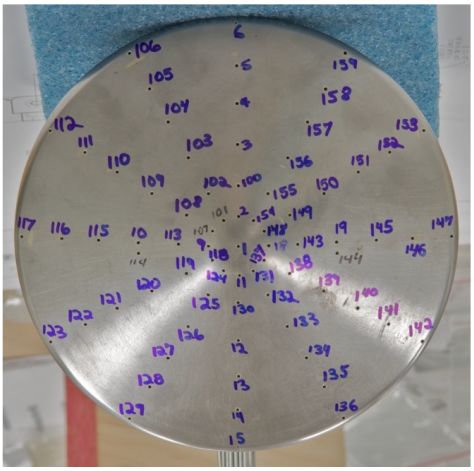

(b) Pressure taps on the forebody from test 1855

Fig. 4 Illustrations of the test hardware for LUPWT tests 1811 and 1855 [Source: NASA].

validation data. The model was instrumented with fifteen static pressure gauges on the forebody, eleven on the aftbody, and eight more on the shoulder. The pressure taps are illustrated in Fig. 4b, though only some of the taps were equipped with static pressure gauges. These tests covered Reynolds numbers from $Re_D = 5 \times 10^5$ to 2×10^6 and Mach numbers from 2.5, 3.5, and 4.5. Repeatability was investigated using several different locations in the tunnel. The LUPWT is known to have slight nonuniformities across the test section due to its 2D sliding-block nozzle. An attempt was made to correct for these bias errors; unfortunately, none of these methods have proven accurate enough to correct the data without inducing unknown errors. Several different positions within the tunnel were used, which resulted in several different experimental values. As a conservative estimate, the experimental uncertainty in this paper is the spread of experimental values, plus the quoted uncertainty in the force and moment balance.

These experimental tests were designed to provide mission-critical validation data for MSL, rather than give a close examination of any particular flow physics. The tests and the aerodynamic database were summarized in Refs. [2, 20, 34], and a subset of the data is shown in Figs. 7 and 8 of Schoenenberger et al. [34]. Nevertheless, these experiments do not meet the full set of requirements for turbulence model validation, such as those requirements outlined by Settles and Dodson [35]. Only surface pressure and aerodynamic coefficients were measured; more sensitive quantities of interest such as skin friction, surface heat transfer, or wake velocities were not measured. There is no experimental data on the size of the separated wake or separation points, both of which would be useful for comparing model predictions. These limitations should be remembered when considering the following validation. Additional wake flow experiments should be funded to meet the specific requirements of turbulence model validation, similar to the low-speed experiments by Ross et al. [36].

A. Quantities of Interest

For Mars entry vehicles, the primary quantities of interest will be the lift-to-drag ratio and the trim angle for a given moment reference point. These are computed using the axial force, normal force, and pitching moment. These forces are defined according to the coordinate frame in Fig. 5. The plots in this paper use the x,y,z coordinates from the body coordinate frame, which is centered at the nose. The pitching moment can be computed at the nose ($x/D = 0$,$y/D = 0$, $z/D = 0$) or at the CG, defined as $x_{cg}/D = 0.3$, $y_{cg}/D = 0$, $z_{cg}/D = 0.0215$.

The desired accuracy of aerodynamic predictions will always be mission specific. However, some generic guidelines can be pulled from previous Mars missions. For MSL aerodatabases [34], the static aerodynamic uncertainties in the supersonic range ($M_\infty < 5$) were:

- $\pm 10\%$ for C_A
- ± 0.01 for C_N
- ± 0.005 for C_m

Kaarlgard et al. [3] compared the preflight predictions of Mars 2020 with the flight data. They found that C_A was predicted to within 2%, and the trim angle-of-attack was predicted to within 0.05 degrees.

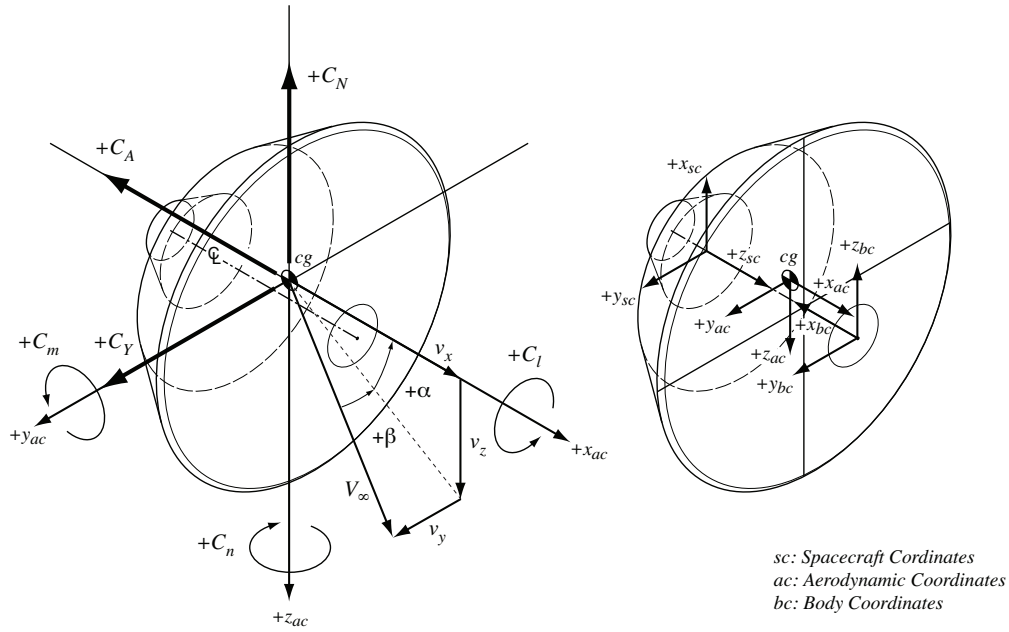

Fig. 5 Definitions for the aerodynamic coefficients, coordinate frames, and moment reference points.

Surface pressure is also examined in this paper, though it only indirectly impacts the lift-to-drag ratio or trim angle. The pressure coefficient is defined as:

$$c_p = \frac{p - p_\infty}{1/2\rho_\infty u_\infty} \tag{1}$$

The surface pressure provides a deeper understanding of where the models have limited accuracy. Integrating coefficients like C_A or C_N can lead to error cancellations, such as positive errors on the forebody masking negative errors on the backshell. It is possible to get the right answer for the wrong reason: integrated coefficients can be predicted accurately, while key turbulent physics are poorly modeled. This was emphasized by Settles and Dodson [35], and demonstrated clearly by Schwing and Candler [8]. Matching experimental data for surface pressure is a more stringent validation test.

III. Computational Setup

This section introduces the computational tools used for the CFD validation. These include FUN3D and Sketch-to-Solution (S2S). The gas models and boundary conditions are also introduced.

A. FUN3D

The studies in this paper use FUN3D, a finite-volume code produced by NASA [37]. FUN3D solves the conservative Favre-averaged Navier-Stokes equations using a median-dual discretization. The inviscid fluxes are discretized using a low-dissipation Roe flux with reconstruction [38], which is second-order accurate. Stencil-based Van Albada limiters were used. The viscous fluxes were discretized using Green-Gauss element-based gradients, which is equivalent to a Galerkin-based approach for regular tetrahedra.

Since comparisons were made primarily to wind tunnel data using air and the maximum Mach number is 4.5, the fluid is treated as a calorically perfect gas. For each of these cases, the walls are modeled with adiabatic and no-slip conditions. The farfield is imposed using Riemann invariants, as described by Carlson et al. [39].

B. Sketch-to-Solution

Grid generation is an important part of CFD, and high-quality solutions usually require high-quality grids. "High quality" can be defined in several ways for blunt-body aerodynamics. First, the grid should be aligned to the bow shock to minimize errors in the numerical fluxes. As shown by Candler et al. [40] and McCloud [28], shock alignment can have significant impacts on solution accuracy. Second, the grid must be fine enough to resolve any gradients in the

solution that will impact the quantities of interest, including boundary layers and isentropic expansions. Finally, the boundary layer should have a relatively fine wall-normal spacing to resolve the viscous sublayer. Turbulence models introduce an additional wall sensitivity, with many turbulence models requiring a wall-normal spacing requirement of $\Delta y^+ \leq 1$ for accurate velocity profiles (see the discussion on flat-plate boundary layers in Ref. [41]). A wall-normal spacing of $\Delta y^+ > 10$ produces unacceptably large errors in skin friction when the turbulence is significant. These errors may be acceptable for low Reynolds number flows or in regions dominated by inviscid effects. Pressure predictions are also less sensitive to the near-wall grid than skin friction.

To help satisfy the mesh requirements in the previous paragraph, this paper makes use of the Sketch-to-Solution (S2S) process [42]. S2S is an iterative process where anisotropic unstructured adaptation is used to convert an initial coarse mesh to a high-quality final mesh. The S2S workflow is pictured in Fig. 6. An initial mesh is generated, and an initial (inaccurate) solution is obtained on the initial mesh. The mesh resolution is measured by the complexity, as defined by Alauzet et al. [44]. For practical use, the complexity is proportional to the number of nodes. The mesh is iteratively adapted and refined using the software tool *refine*, with several adaptation cycles occurring at a given mesh complexity before increasing the resolution. Usually, the cycle of adaptation and refinement is continued until a predefined complexity limit is reached.

The S2S process can be used with multiscale metric adaptation. Multiscale mesh adaptation attempts to minimize the L_2 norm of the interpolation error of a scalar field such as temperature or Mach number. After running the CFD solver and generating an output scalar field, the Hessian of the target scalar field is calculated. This Hessian is then decomposed into eigenvalues and eigenvectors. A Riemannian metric tensor is formed by recombining the inverse square of the eigenvalues with the eigenvectors to ensure a symmetric, positive-definite metric; the metric is then used to construct an anisotropic grid. For further details, see Refs. [44–46].

IV. Comparison of Mesh Generation Techniques

As mentioned in the introduction, several opposing trends have emerged in the recent decade concerning mesh adaptation for high-speed flows. A frozen, prismatic boundary-layer mesh is sometimes used alongside mesh adaptation, such as in Refs. [23, 24, 29]. Also, the optimal choice of scalar field is not clear a priori, and several choices have been made in previous projects (see Refs. [23, 24, 29, 47]). These include temperature and Mach number.

In order to remove some complexity, the different gridding options were studied on a simpler problem. Only the heatshield and bow shock were considered, with the computational domain terminating at the shoulder. This domain and geometry are pictured in Fig. 7. The backshell was not included both due to its geometric complexity and because mesh requirements are more clear for boundary layers than for separated wakes.

Only a single set of freestream conditions were examined: Mach 2.5, $Re_D = 10^6$, $\alpha = -16°$, and $T_\infty = 144K$. These conditions correspond to a case from the LUPWT tests, but no comparison is made here. Since the backshell has a significant effect on axial and normal forces, the forebody-only geometry complicates any such comparison. The boundary conditions used for the forebody only cases are identical to those used for the full geometry. The heatshield is

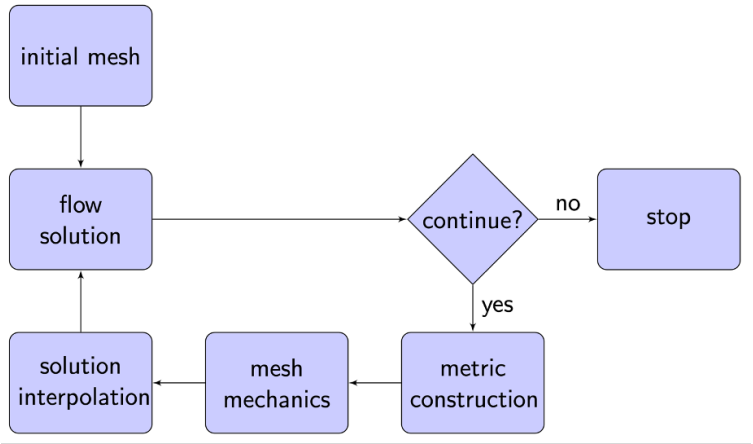

Fig. 6 Grid adaptation process when using S2S (from Park et al. [43]).

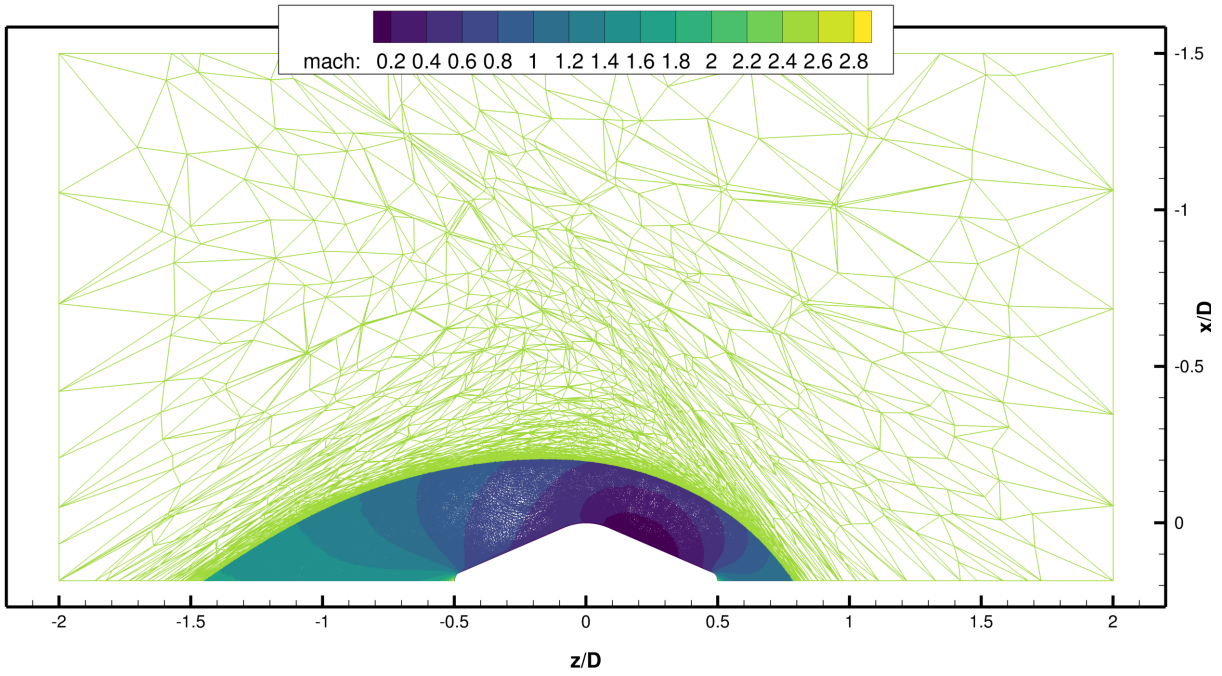

Fig. 7 Computational domain and final adapted grid for the forebody-only cases. This grid corresponds to Mach 2.5, $Re_D = 10^6$, $\alpha = -16°$ case, and a resolution of approximately 32 million nodes.

treated as an adiabatic, no-slip wall. The inflow boundary and the sides are imposed using Riemann invariants. The outflow boundary automatically switches between subsonic and supersonic boundary conditions: for the subsonic region, a pressure-based outflow is imposed using Riemann invariants, while the supersonic region uses an extrapolation.

Five grid generation approaches were tested for the following work, split into three categories and three approaches within the first category:

1) **Fully tetrahedral**: In this approach the grid is composed entirely of tetrahedra. Sketch-to-solution [42] is used to iteratively adapt the grid. The entire mesh is adapted, including the surface mesh, the mesh in the boundary layer, and the mesh near the bow shock. An example surface mesh is shown in Fig. 8a. A slice through a volume mesh is shown in Fig. 9a. For the fully tetrahedral mesh, three different scalar fields were examined:
   (a) Mach number
   (b) Temperature
   (c) Total enthalpy

   Density was also briefly examined, but had some of the same problems with near-wall spacing as temperature, which will be discussed later. Total enthalpy may seem questionable for adaptation, since total enthalpy is constant across a stationary shock wave. However, most shock-capturing algorithms only conserve total enthalpy if the grid is aligned with a shock wave. When a grid is not aligned with a shock wave, a Roe-type scheme will not conserve total enthalpy and gradients appear. This guides the grid adaptation toward refinement and alignment at the shock.
2) **Structured, hexahedral boundary layer**: The surface grid for the MSL forebody is generated by hand, using expert guidance. The resolution is based on the previous meshes used for the MSL database [2]. The surface mesh can be seen in Fig. 8b, and a slice through a volume mesh can be seen in 9b. A prismatic boundary layer is then extruded from the body using the Pointwise® T-Rex method. A stretching ratio of 1.15 was used with up to 30 prismatic layers. The first wall-normal distance was defined such that $\Delta y^+ < 1$ for all points. Beyond the prismatic boundary layer grid, tetrahedra are used to mesh the external flow. This mesh also requires adaptation using S2S, in order to align the tetrahedral portion of the mesh with the bow shock and improve resolution of the gradients outside the boundary layer. The boundary layer mesh remained frozen through the S2S refinement and

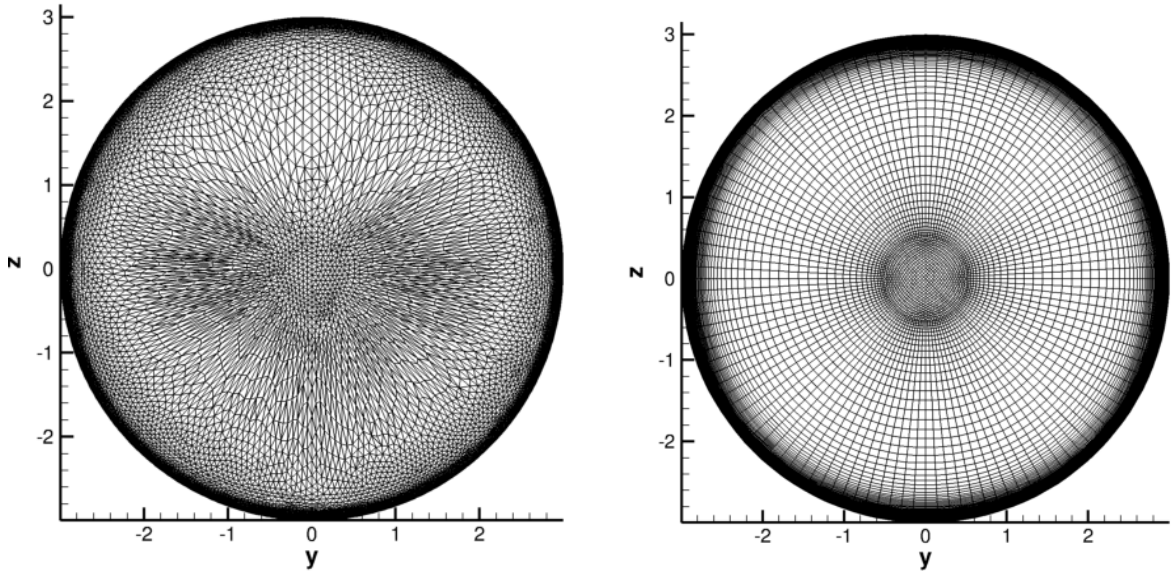

(a) Adapted, triangular surface mesh **(b) Manual, quadrilateral surface mesh**

Fig. 8 Visual comparison of the two types of surface meshes: (a) An adapted surface mesh made with triangles, and (b) a manually crafted surface mesh made with quadrilaterals. The surface grids have 12,403 and 13,441 nodes, respectively. The adapted mesh shown is not from the final mesh, but from an intermediate mesh refinement that more closely matches grid (b) in surface resolution.

adaptation cycles. This is similar to the technique used by Nastac et al. [29].

3) **Unstructured, triangular prism boundary layer**: Instead of expert guidance, this approach uses S2S to define an appropriate surface mesh. After running the fully tetrahedral case, the surface mesh is extracted from the final grid. This surface mesh is then used to generate a prismatic boundary layer, composed mainly of triangular prisms. Aside from the surface generation technique, the rest of the mesh creation proceeded as in the previous approach. Pointwise® was used to generate the initial grid, while S2S was used to adapt and refine the mesh outside the boundary layer. A slice through the volume mesh can be seen in Fig. 9c.

Considering all options, there are five total approaches, labeled 1a, 1b, 1c, 2, and 3 above. These five approaches share several important similarities and differences. All five techniques use *refine* to adapt the grid to the bow shock and gradients in the external flow. The number of nodes in the final adapted meshes are similar between all three cases. However, the surface grid and boundary layer mesh resolution were different. The manually created surface grid was based on previous grids used for Mars flight programs, but was coarser than the final surface mesh from the purely tetrahedral mesh. Manually creating a more fine structured surface mesh was not attempted. Because the prismatic boundary layer extrusion stopped when cells became approximately isotropic, the larger grid spacing in the manually created mesh resulted in a thicker boundary layer grid.

The fully tetrahedral meshes started with a coarse resolution of 295,000 nodes. Because of the frozen boundary layer meshes, the meshes with hexahedral and triangular prisms started with different node counts of 600,000 and 10 million, respectively. The higher starting node count for the triangular prism boundary layer mesh is due to a fine surface grid on even the coarsest mesh. For all five approaches, the tetrahedral portion of the mesh was adapted several times at each complexity level, then refined after four iterations or when the drag differed by less than 1% (whichever occurred first). The complexity of the tetrahedral region was doubled in each refinement, which corresponds roughly doubling the number of nodes in the tetrahedral region. This sequence of grids is shown in Fig. 10.

A. Results

The predictions of axial force, normal force, pitching moment, and lift-to-drag ratio are depicted in Fig. 11. While in S2S, the grid is adapted several times at a given complexity level, only the results from the final grid adaptation at each complexity level are shown. There are small differences in the predicted aerodynamic coefficients, even at the finest

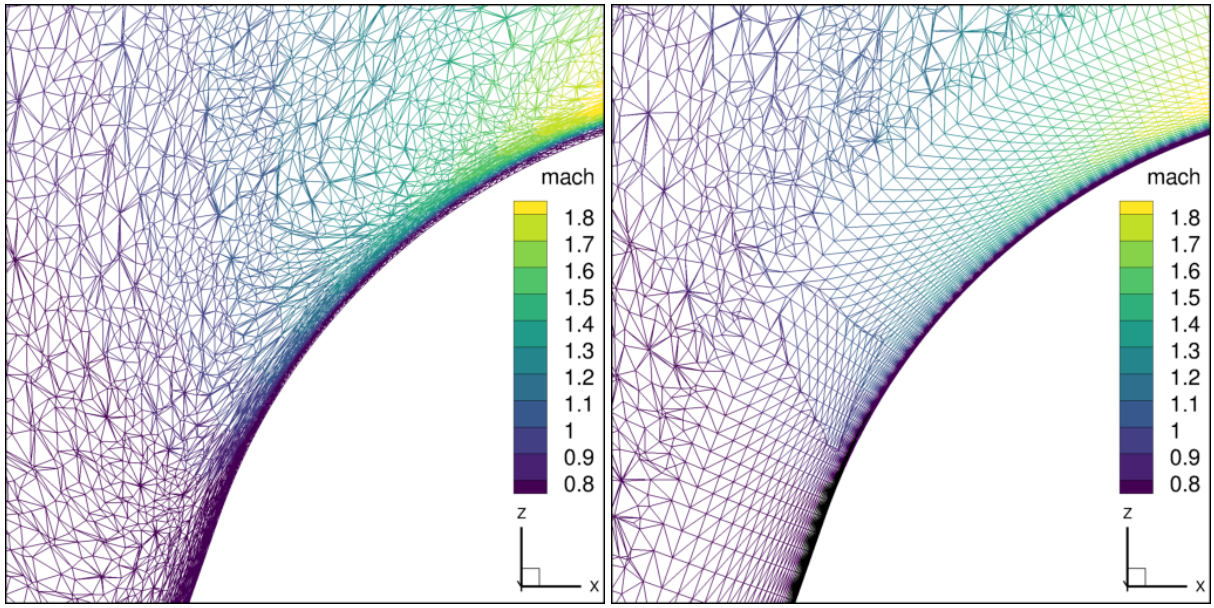

(a) Fully tetrahedral mesh **(b) Structured, hexahedral boundary layer**

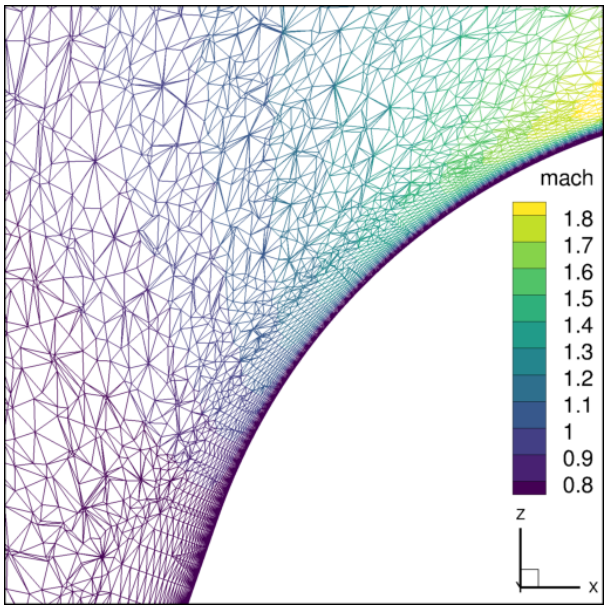

(c) Unstructured, triangular prism boundary layer

Fig. 9 Slices through the volume mesh for various different mesh generation techniques. These solutions were run at Mach 2.5, $\alpha = -16°$.

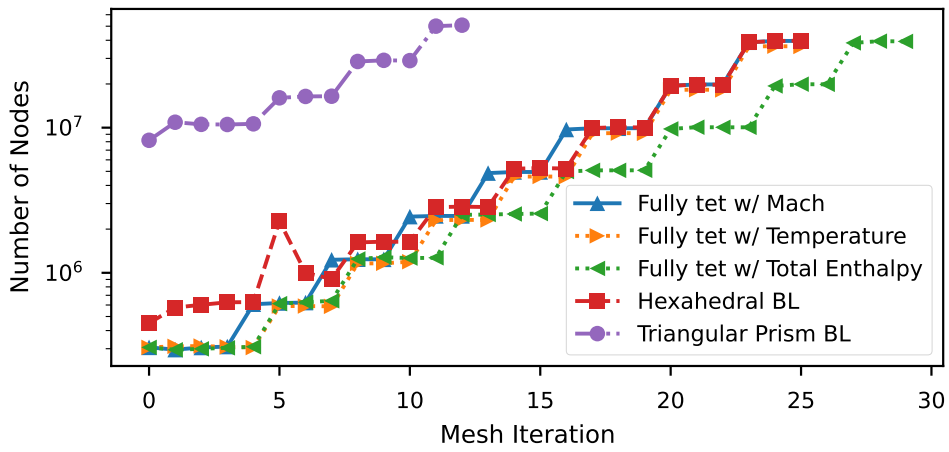

Fig. 10 Refinement of the meshes used for the mesh sensitivity analysis. The fully tetrahedral meshes are adapted using Mach number, temperature, or total enthalpy as a target scalar field.

resolution. Compared with the uncertainties for previous missions, these differences are relatively small. The predicted axial force differs by 0.5% or less, which is smaller than the actual error of 2% seen in the post-flight reconstruction of Mars 2020 [3]. The other sensitivities and uncertainties are compared in Table 1. With a fine enough grid, there are only small differences in predicted lift or drag between a prismatic boundary layer and a fully tetrahedral grid. There are larger sensitivities to consider, such as the turbulence model in the separated wake.

There is a surprising dependence on the surface and boundary layer mesh. The two different frozen boundary layer mesh approaches give slightly different predictions, even in the fine grid limit. This is especially true for the normal force, C_N, where the triangular prism BL mesh consistently predicts a higher force that is not in family with the other predictions. This illustrates a danger of the "frozen boundary layer" approaches. Any grid with finite resolution will have some discretization error. By neither refining nor adapting the boundary layer grid, that discretization error is fixed and will not decrease. Ideally, the boundary layer grid should also be adapted and refined, but this introduces an additional set of independent variables (e.g., surface spacing or wall-normal spacing). Most studies combining a frozen boundary layer approach and anisotropic mesh adaptation do not demonstrate refinement of both regions of the mesh.

Comparisons can also be made between the three different scalar fields for the interpolation-error-based anisotropic adaptation. In the fine-grid limit of 32 million nodes, all three grids give similar predictions, and differences are much smaller than desired uncertainties. However, there are larger difference on the coarse grids, even after several cycles of adaptation and refinement. Total enthalpy, in particular, requires a larger number of nodes before it comes into agreement with the other solutions.

Some of these differences on coarse meshes may be attributed to the near-wall mesh. In a problem with a boundary layer and a bow shock, the grid resolution must be balanced between these two different flow features. Despite its merits, anisotropic mesh adaptation (as currently practiced) tends to overemphasize refinement of the shock and underemphasize refinement of the boundary layer. This occurs because the boundary layer has finite gradients and Hessians, while the analytical definition of a shock is discontinuous. While shock-capturing schemes will lead to some numerical dissipation

Table 1 Comparison of the grid sensitivity to the uncertainty and error from previous Mars missions. Grid sensitivity refers to the spread in predictions, depending on the mesh generation technique.

	C_A	C_N	C_m
Grid Sensitivity	±0.25%	±0.0011	$\pm 3.6 \times 10^{-4}$
MSL Aerodatabase Uncertainty	±10%	±0.01	$\pm 5.0 \times 10^{-3}$
Mars 2020 Accuracy	±2%	-	-

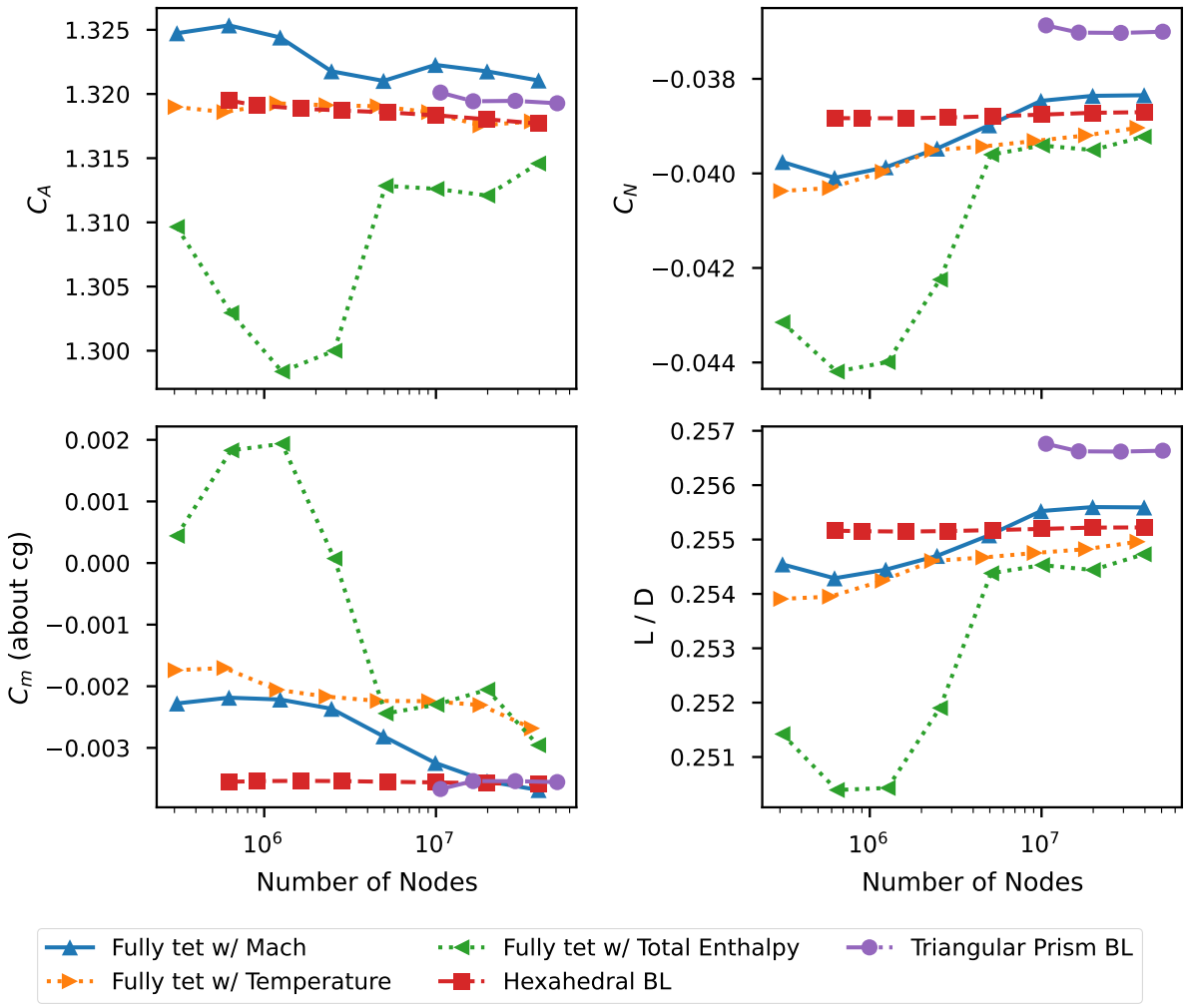

Fig. 11 Aerodynamic coefficients predicted for the forebody as a function of the grid resolution. The fully tetrahedral meshes are adapted using Mach number, temperature, or total enthalpy as a target scalar field. Only the results from the final mesh adaptation at a given mesh complexity are shown.

and a finite shock width, this width is dependent on the grid. Finer grids lead to larger Hessians; the eigenvalues of these Hessians are much larger than the eigenvalues of the Hessian in a boundary layer. This imbalance occurs due to the feedback between the shock-capturing schemes in the CFD solver and *refine*. According to the anisotropic mesh adaptation algorithm, the grid optimally minimizes the interpolation error metric in each scalar field.

As shown in Fig. 12, the near-wall resolution was relatively coarse for grids without a manual, prismatic boundary layer. This figure depicts the Δy^+, which is defined as:

$$\Delta y^+ = \Delta y \sqrt{\tau_w / \rho_w} / \nu_w \tag{2}$$

where Δy is the height of the first cell at the wall, τ_w is the wall shear stress, ρ_w is the density at the wall, and ν_w is the kinematic viscosity at the wall. The accuracy of the computed value of Δy^+ can be questioned. Coarser grids can lead to errors in τ_w, which propagate to errors in Δy^+. However, correcting the Δy^+ calculation with a more accurate value of τ_w did not significantly decrease the computed values of Δy^+. In general, none of the methods create meshes with $\Delta y^+ \leq 1$. Temperature is the worst for wall-normal resolution, creating values as large as $\Delta y^+ = 65$. The adiabatic wall boundary condition leads to very small eigenvalues of the Hessian near the wall, which leads to large wall-spacing. The results may change for different wall boundary conditions. Total enthalpy is not consistently better than temperature, with values as large as $\Delta y^+ = 20$. Mach performs the best, with values less than 10 across most of the forebody.

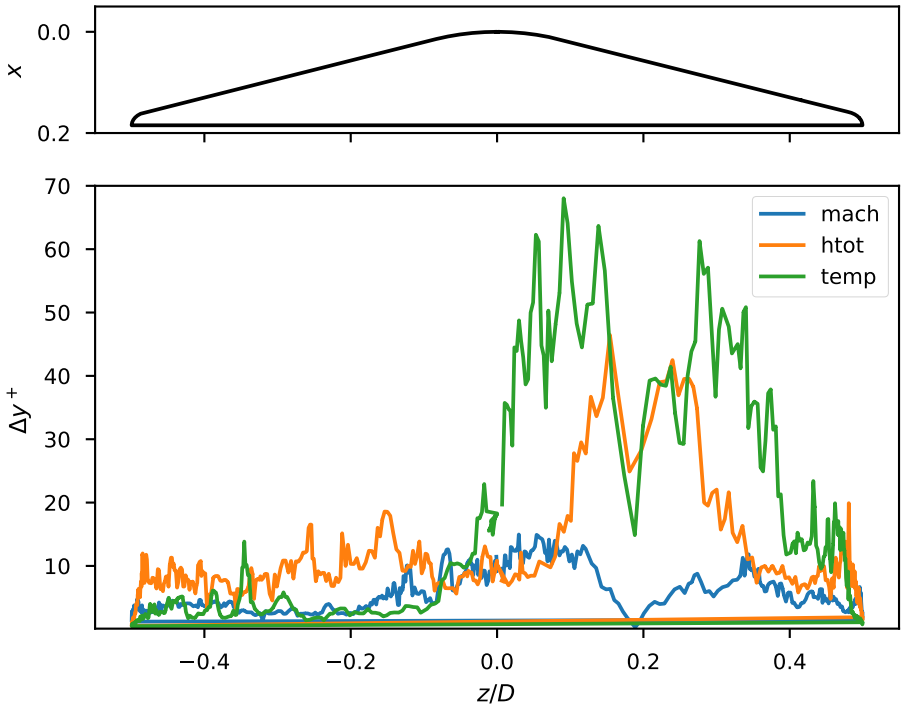

Fig. 12 The wall-normal grid spacing for the finest mesh of an adaptation cycle for three scalar fields. A diagram of the heatshield geometry is included for reference. Using temperature for the scalar field creates large values of Δy^+, and Mach provides the smallest values. The stagnation point is around $z/D = 0.19$

While these results may improve under grid refinement, a grid of 32 million nodes is already excessive for a relatively simple geometry. Meshing a smooth forebody with more than 32 million grid points is not common. For more complex geometries, such as modeling the reaction control jets, fine grid resolution will be needed for finer geometry features and resolving the turbulent jets. Requiring more than 32 million nodes for simple geometries (such as a 70 degree sphere-cone) will result in an excessive computational cost.

If fully tetrahedral meshes are to be used, without prismatic boundary layers, the Mach number yields the best boundary layer refinement. Temperature and density should be avoided when using adiabatic wall boundary conditions. Additional research should be conducted on how to better balance grid adaptation across shocks and boundary layers.

Despite these concerns, it is worth repeating that the differences between mesh generation techniques are generally small for integrated quantities when compared to the uncertainty carried by previous Mars entry vehicles. The discretization error is just a part of the overall error, and as shown in Section V, turbulence modeling is a larger contributor to prediction errors. These results *do not* suggest that discretization error is insignificant for a flight project. It is always possible to create a bad mesh with a high discretization error. The results suggest instead that meshing best practices help minimize sensitivity to the mesh. In the current work, the surface mesh for the hexahedral mesh was created using best practices, and the other surface meshes were much finer. These results suggest that discretization error can be small when best practices are followed, the mesh is adapted, and the grids are sufficiently fine.

V. Turbulence Modeling Sensitivities

The second validation study in this paper examines predictions of the full MSL wind tunnel model, including the backshell and a 30-degree sting. For both the LUPWT experiments and the CFD, a simplified version of the flight geometry was used, designated internally as OML–13F. The differences between this shape and the flight vehicle are mainly due to small variances in TPS thickness near the shoulder area that produce negligible effects on the forces and moments acting on the vehicle. A small groove where the heatshield joins the backshell has been smoothed over in the CFD model. This geometry is shown in Figs. 1 and 13a. The sting is an important feature, since it fundamentally changes the wake. When the experiment was designed, efforts were made to minimize the impact of the sting by aligning it with the nominal trim angle. However, the sting will always impose a no-slip boundary inside the wake, which is not present in a free-flight configuration. This boundary changes the wake velocities and therefore the wake closure. There is some uncertainty about extrapolation to flight conditions. Nevertheless, the abundant wind tunnel data for this geometry makes it a valuable validation case.

The previous section examined the sensitivity of the aerodynamic coefficients to gridding strategies, especially with respect to a prismatic boundary layer mesh. Since the mesh sensitivity was much smaller than the experimental uncertainties, the mesh sensitivity is not considered in this section. Interactions between the mesh adaptation and the turbulence model were not examined. Four separate turbulence models were examined:

1) **SA-neg**: This is a Spalart-Allmaras model described by Allmaras et al. [48]. The "-neg" portion of the model improves robustness over the original SA model, but should not affect converged solutions. This is abbreviated as **"SA"** in the figures.
2) **SA-neg-RC-QCR2000**: This is a Spalart-Allmaras model with Rotation-Curvature corrections [49] and a Quadratic Constitutive Relationship [50]. For brevity, this model is referred to as **"SA-RC-QCR"** in the figures.
3) **SA-comp**: This variation includes a compressibility correction by Spalart [51]. This correction was designed to reduce the eddy viscosity in compressible shear layers, such as those around the wake of the MSL.
4) **SST**: This is the Shear Stress Transport model by Menter [52]. Unlike the Spalart-Allmaras family of models, this is a two-equation model.

While some LUPWT tests were performed at $Re_D = 5 \times 10^5$ and $Re_D = 2 \times 10^6$, the majority of the test data is in the range $Re_D = 10^6$. The freestream conditions were set to the following:

- Mach 2.5, $Re_D = 10^6$, $T_\infty = 144.4\,\mathrm{K}$
- Mach 3.5, $Re_D = 10^6$, $T_\infty = 98.2\,\mathrm{K}$
- Mach 4.5, $Re_D = 10^6$, $T_\infty = 67.1\,\mathrm{K}$

For each Mach number, four angles of attack were examined: $\alpha \in \{0°, -16°, -24°, -32°\}$. The $\alpha = -16°$ case is close to the trim angle for a moment reference point of $x_{cg}/D = 0.3$, $z_{cg}/D = 0.0215$, and has the least interference from the sting. The higher angle-of-attack cases show significant flow-reattachment on the windward side. The $\alpha = 0°$ case is not axisymmetric due to the presence of the sting.

The next subsection summarizes the computational grid and explains the choice of final resolution. The subsequent subsections cover the validation results at Mach 2.5, 3.5, and 4.5. The focus is primarily on Mach 2.5, since the integrated coefficients are most sensitive to the turbulence model at lower Mach numbers.

A. Grid Generation and Computational Domain

A spherical farfield of radius $r/D = 5$ is imposed around the vehicle centered at $x/D = 3.5$, $y/D = -0.5$. The computational domain is depicted in Fig. 13a. The domain was intentionally coarsened downstream of the vehicle at the outer boundary, in order to decrease unnecessary grid refinement and act as a sponge layer. While these cases were steady, the initial transients can lead to resolved vortices and reverse flow at the outflow boundary if the mesh is highly resolved there.

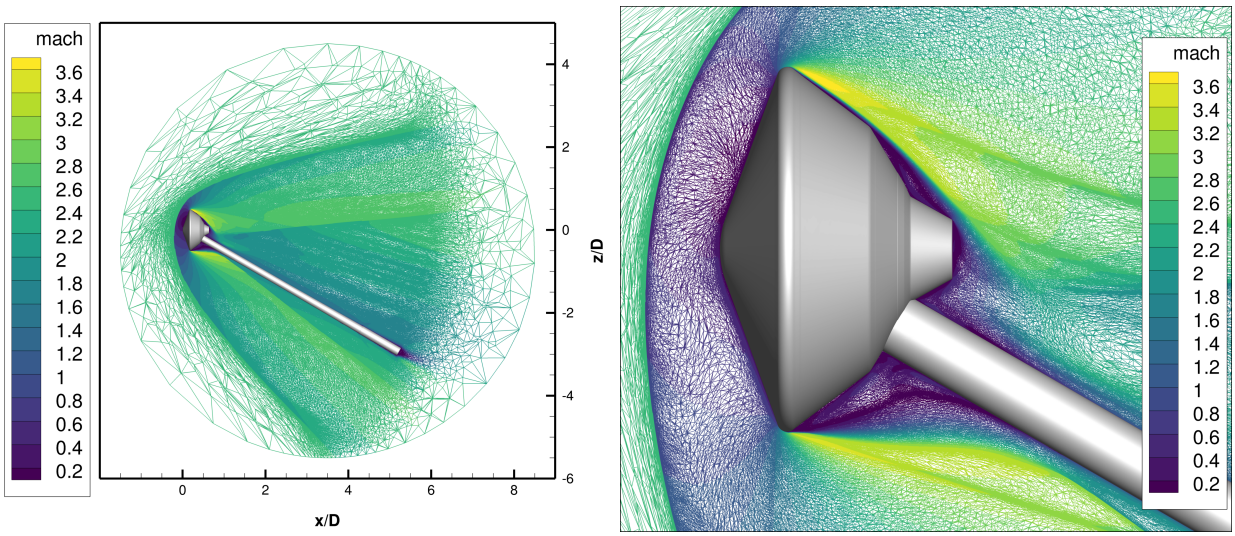

(a) A slice of the full computational domain **(b) Closeup of the grid around the capsule**

Fig. 13 Visualization of the domain and mesh for the full-vehicle simulations at a resolution of approximately 32 million nodes, Mach 2.5, and $\alpha = -16°$.

Sketch-to-Solution (S2S) was used to generate and adapt the mesh with a purely tetrahedral grid, as described in Section III.B. Prismatic boundary layer grids were not used. The initial mesh contained approximately 4 million nodes, and the mesh was iteratively adapted until reaching 32 million nodes. An example mesh refinement is depicted in Fig. 14. The Mach number was used as the scalar field for the error-based adaptation.

There is some question as to the necessary resolution for capsule wake-flow problems. For the MEDLI2 ballistic tests in Refs. [14, 21], the US3D grid used 20 million nodes and the OVERFLOW grids used 36 million nodes. Ekelschot et al. used 32 million nodes for their post-flight deep dive on MEDLI2 [9]. After examining the predicted aerodynamic coefficients, 32 million nodes was considered sufficient. As an example, the changes in the aerodynamic coefficients during refinement is depicted in Fig. 15 for a Mach 2.5, $Re_D = 10^6$, $\alpha = -16°$ case. The experimental results, including uncertainty bounds, are also shown for comparison. The changes in all coefficients between 16 and 32 million nodes are smaller than the experimental uncertainty. The axial coefficient (C_A) is overpredicted for SA and SA-RC-QCR2000, but there is no indication that increased mesh resolution will lower the errors. The pitching moment may change with increased resolution, but the changes from mesh to mesh are still much smaller than the experimental uncertainty. Based on these results, a 32 million node mesh is considered adequate for prediction of aerodynamic coefficients using S2S.

The relatively small changes between 16 and 32 million nodes give some assurance about the quality of the solution. However, this should not be confused for a formal estimate of discretization error. An attempt was made to quantify grid discretization error with the Grid Convergence Index of Roache [53, 54]. The same metric field was used to generate an unstructured "grid family" of 8 million, 16 million, and 32 million nodes. The solution on these meshes was compared to a finer, 64 million node solution. Unfortunately, the estimated error did not bound the fine-mesh predictions of aerodynamic coefficients without introducing large safety factors. Further research should be conducted into estimating discretization error using multiscale anisotropic mesh refinement.

B. Mach 2.5

The Mach 2.5 cases are examined first, and in the most detail. The backshell contributions to aerodynamic forces are most significant at lower Mach numbers, which makes the Mach 2.5 data a more discriminating test case. The experimental data also have larger uncertainties at higher Mach numbers.

Predictions of the aerodynamic coefficients are plotted in Fig. 16. Given the history of poor predictions from RANS models in separated wakes, the integrated coefficients are predicted surprisingly well. The axial force is consistently at the high end of experimental values, or overpredicted by 1–2%. The normal force is underpredicted at $\alpha = -32°$ by 0.002 for SST and 0.004 for SA-RC-QCR2000, but is relatively accurate across the other angles of attack. There is a "knee" in both the experimental and CFD values for C_N around $\alpha = -20°$, where C_N breaks from a straight line and

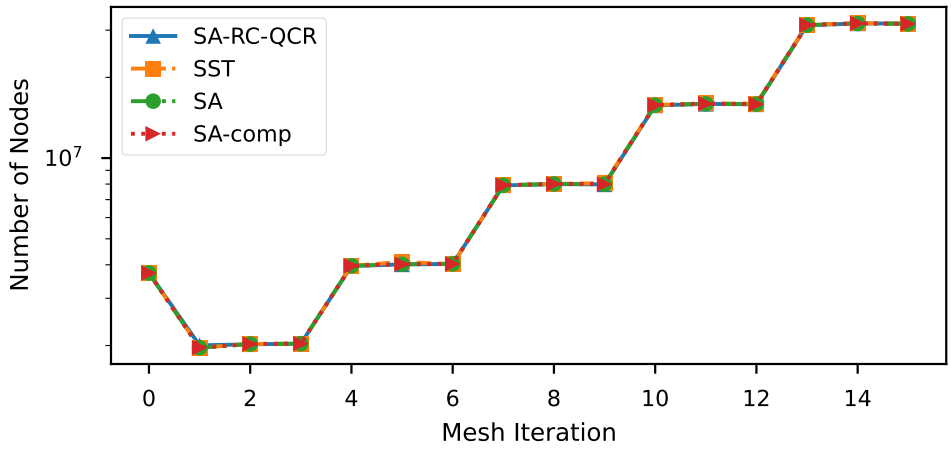

Fig. 14 Grid refinement steps for the full-vehicle simulations.

is lower at higher angles of attack. As shown in the following paragraphs, this can be attributed to attached flow on the windward side of the backshell. The pitching moment is predicted relatively accurately, and is less sensitive to turbulence modeling choices.

Deeper insights can be gained by examining the pressure distribution across the vehicle. Experimental data from the pressure taps are compared with model predictions in Fig. 17–20. The forebody pressures are predicted well, with a median relative error of 0.54%. The effects of angle-of-attack are accurately predicted for the forebody, with the asymmetrical distributions at $\alpha = -24°$ and $\alpha = -32°$ matched by all models. The relatively coarse wall-normal spacings described in Section IV do not appear to significantly limit the accuracy since forebody pressure is dominated by the inviscid effects, with the viscous boundary layer having only secondary effects. Since these forebody pressures are much larger than the backshell pressures, the integrated aero is predicted relatively well.

Unfortunately, the good agreement on the forebody masks the poor predictions of RANS models across the backshell. A closeup of the backshell pressures is included in Fig. 21. For the majority of the backshell, there is a consistent bias error, where the backshell pressure is underpredicted. This is consistent with known deficiencies in RANS models of compressible shear layers. Conventional RANS models overpredict the thickness of the separated shear layer, which leads to a smaller recirculation region and a lower pressure. The underprediction of pressure leads to larger wake drag, which matches the overprediction of C_A.

In separated regions, the RANS models also predict a qualitatively different solution. Examining the $\alpha = 0°$ or the $\alpha = -16°$ solutions in Fig. 21a or 21b, the CFD predicts sharp variations in c_p across the backshell. These stand in contrast to the flatter profile in the experimental pressure. These pressure variations do not correspond to regions of attached and separated boundary layers; these slope changes also occur at $\alpha = 0°$, where the separation occurs only at the shoulder and the whole backshell is separated.

At higher angles of attack, including $\alpha = -24°$ and $\alpha = -32°$, the windward side of the backshell shows larger sections of attached flow. The flow along the first cone is attached on the windward side ($z/D > 0$). This is illustrated in Fig. 22. This attached boundary layer detaches at the bend around the second cone, then impinges on the parachute cover around $z/D = 0.1$. The pressure is higher in these attached flow regions, which is clearly seen in the experimental data of Fig. 21. The pressure taps at $z/D \approx 0.1$ and $z/D \approx 0.4$ correspond to the high-pressure regions on the parachute cover and first cone, respectively. These attached flow regions decrease C_N at high angles of attack, described previously as a "knee" in the experimental data.

Accurately modeling the attached flow is necessary to predict this trend in C_N; an empirical, uniform backshell pressure will not capture this effect. The predictive accuracy of the RANS models in these attached flow regions is mixed. All RANS models match the qualitative trends of increased pressure in attached regions and decreased pressure in the separated regions. However, all models underpredict the pressure in the attached region of the first cone at $\alpha = -24°$, then overpredict the pressure at $\alpha = -32°$.

There is some indication that the SST model performs better than SA-based models in predicting C_A, though the same qualitative errors are present. Overall, none of the "improvements" to the original SA model bring the backshell

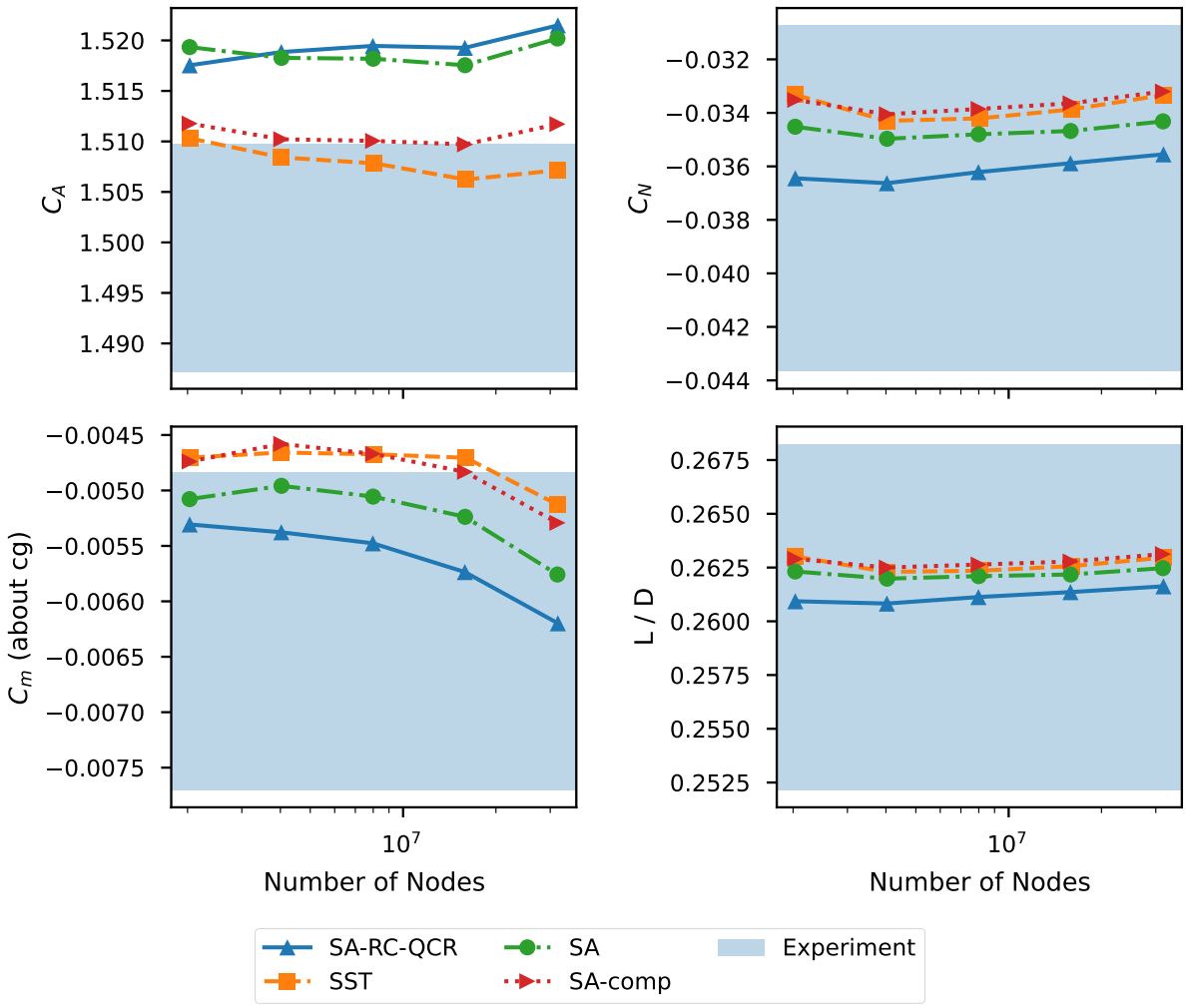

Fig. 15 Change in the predicted aerodynamic coefficients with mesh resolution, for a Mach 2.5, $\alpha = -16°$ case. The experimental value, with uncertainty, is indicated by the shaded region. Only the results from the final mesh adaptation at a given mesh complexity are shown.

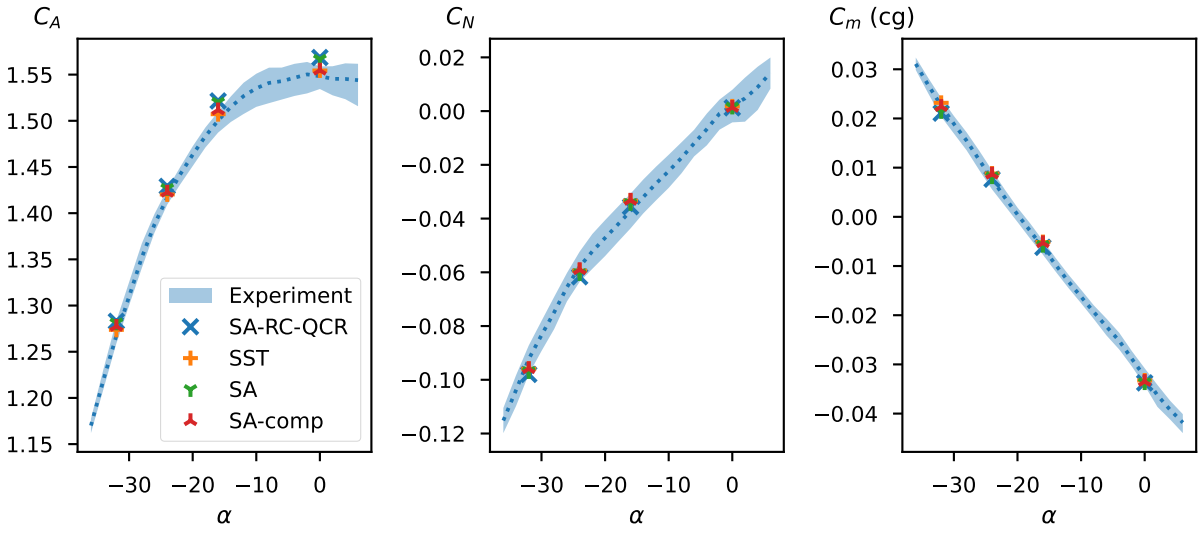

Fig. 16 Comparison of predicted aerodynamic coefficients with experimental data for the Mach 2.5 cases. The experimental data, with uncertainty, is indicated by the shaded regions.

Table 2 Predictions of the aerodynamic coefficients for various turbulence models, at Mach 2.5. These data match Fig. 16.

Coefficient	α [°]	Exp. Min	Exp. Max	SA	SA-RC-QCR	SA-comp	SST
C_A	-32	1.259	1.284	1.281	1.283	1.277	1.274
C_A	-24	1.409	1.426	1.427	1.429	1.423	1.420
C_A	-16	1.487	1.510	1.520	1.521	1.512	1.507
C_A	0	1.534	1.559	1.567	1.569	1.555	1.554
C_N	-32	-9.79e-02	-8.72e-02	-9.69e-02	-9.80e-02	-9.59e-02	-9.59e-02
C_N	-24	-6.35e-02	-5.23e-02	-6.04e-02	-6.17e-02	-5.90e-02	-5.94e-02
C_N	-16	-4.37e-02	-3.07e-02	-3.43e-02	-3.56e-02	-3.32e-02	-3.33e-02
C_N	0	-4.20e-03	7.93e-03	1.54e-03	1.23e-03	1.34e-03	1.76e-03
C_m (cg)	-32	2.04e-02	2.42e-02	2.14e-02	2.11e-02	2.24e-02	2.32e-02
C_m (cg)	-24	5.58e-03	9.45e-03	8.18e-03	7.65e-03	8.67e-03	8.81e-03
C_m (cg)	-16	-7.70e-03	-4.83e-03	-5.76e-03	-6.20e-03	-5.29e-03	-5.13e-03
C_m (cg)	0	-3.43e-02	-3.08e-02	-3.37e-02	-3.38e-02	-3.35e-02	-3.33e-02

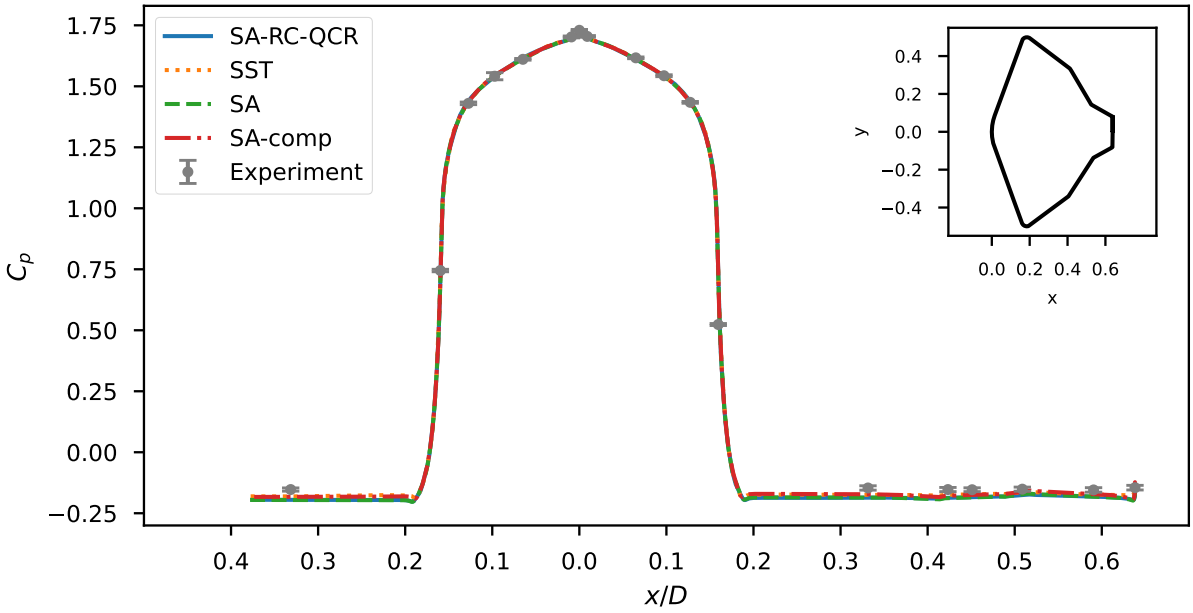

Fig. 17 Pressures along the symmetry plane, at Mach 2.5 and $\alpha = 0°$.

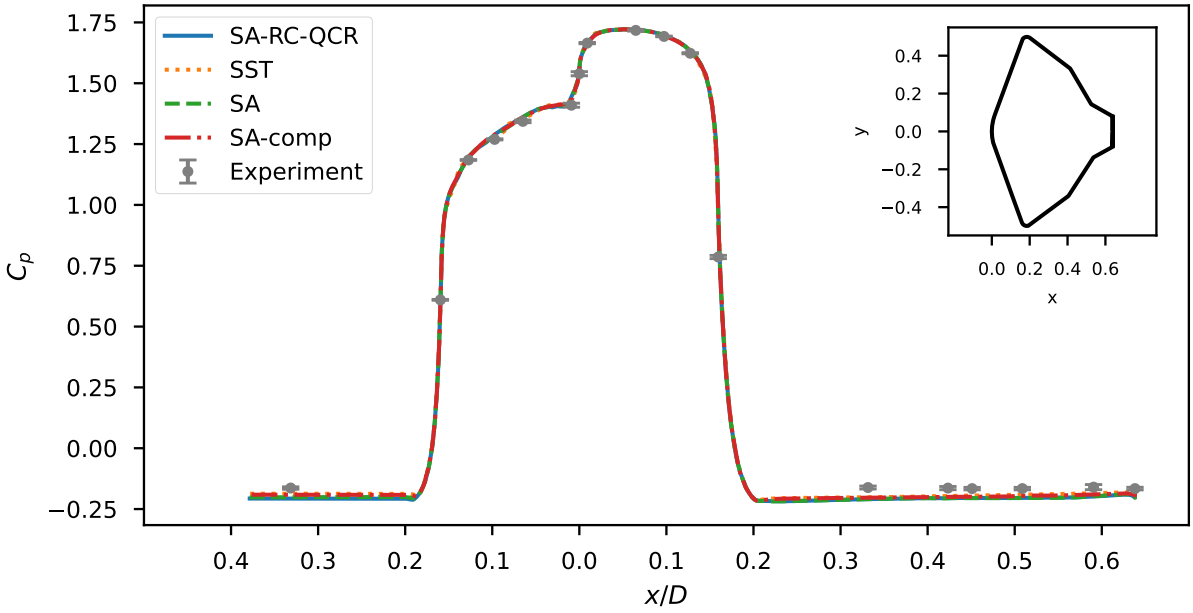

Fig. 18 Pressures along the symmetry plane, at Mach 2.5 and $\alpha = -16°$.

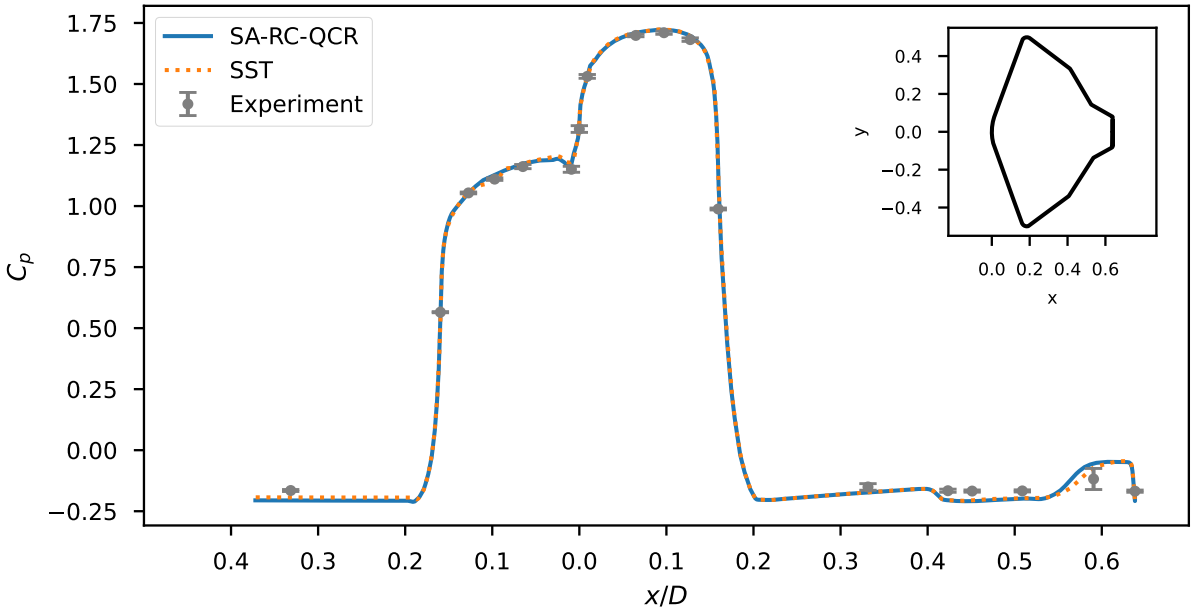

Fig. 19 Pressures along the symmetry plane, at Mach 2.5 and $\alpha = -24°$.

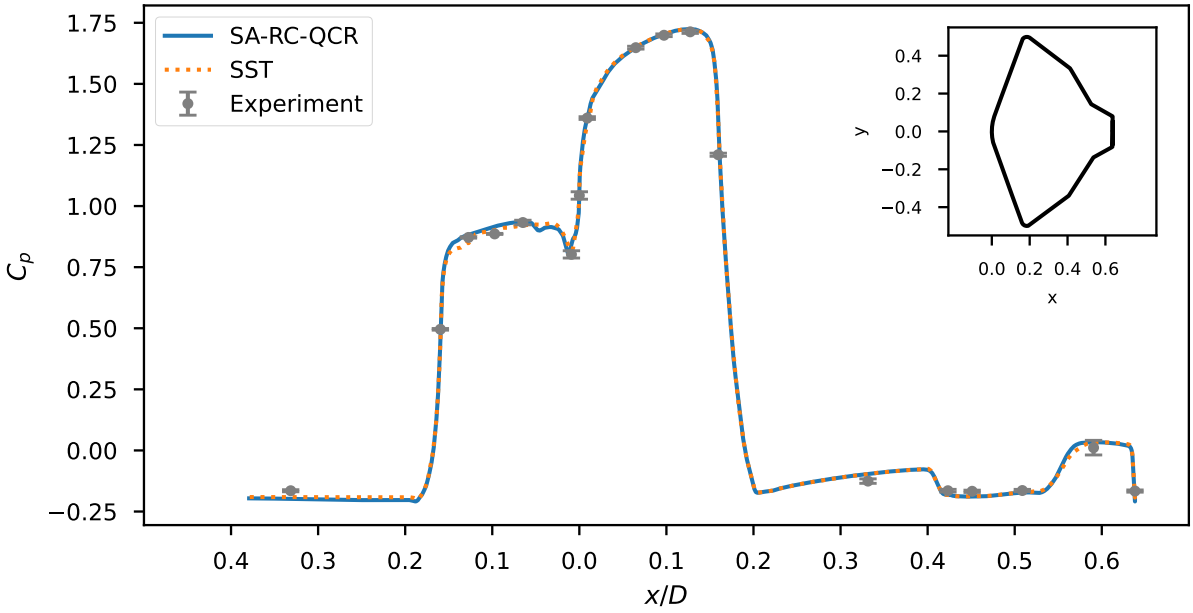

Fig. 20 Pressures along the symmetry plane, at Mach 2.5 and $bm\alpha = -32°$.

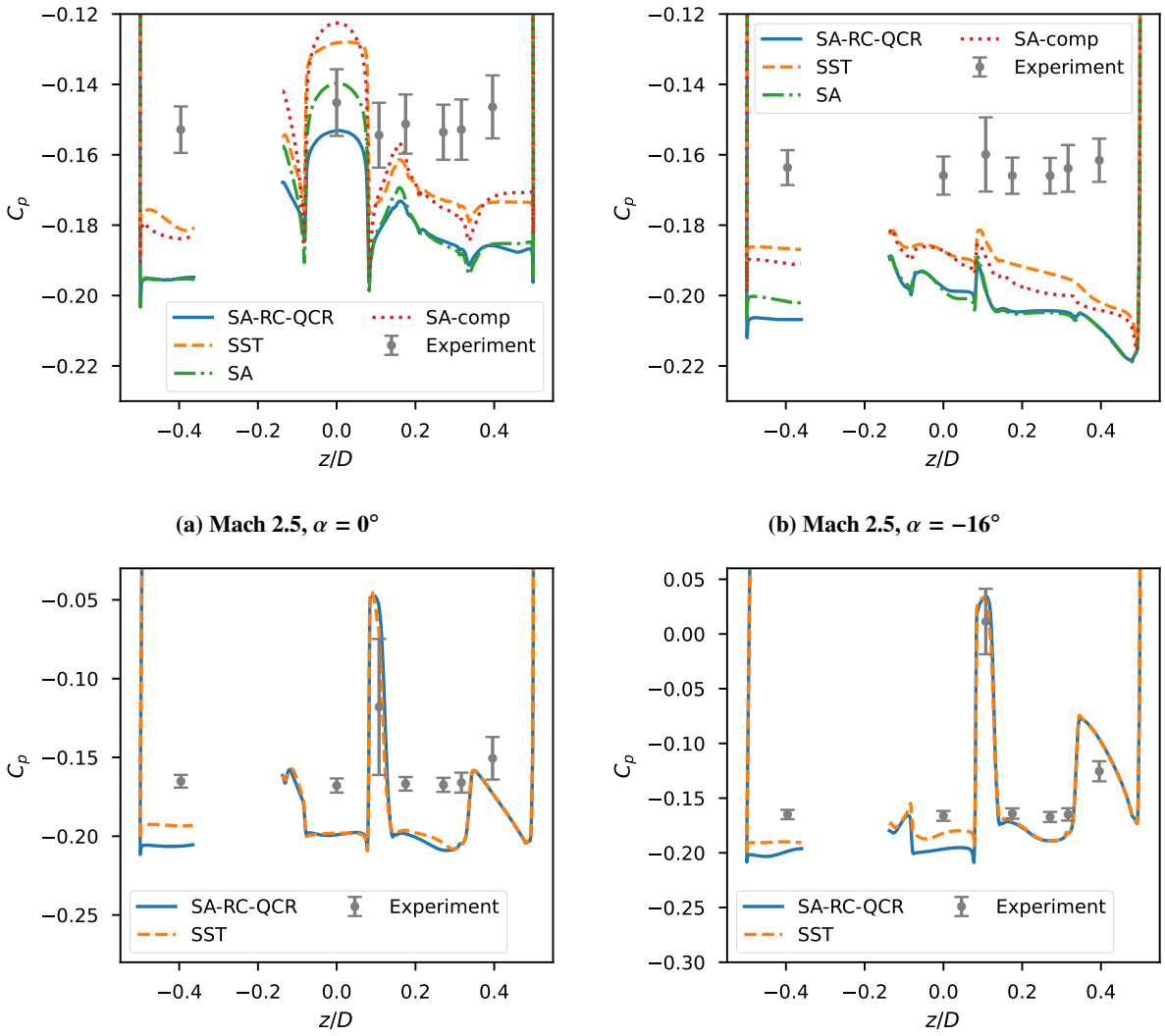

(a) Mach 2.5, $\alpha = 0°$

(b) Mach 2.5, $\alpha = -16°$

(c) Mach 2.5, $\alpha = -24°$

(d) Mach 2.5, $\alpha = -32°$

Fig. 21 Comparison of the predicted surface pressure and experimental data on the backshell.

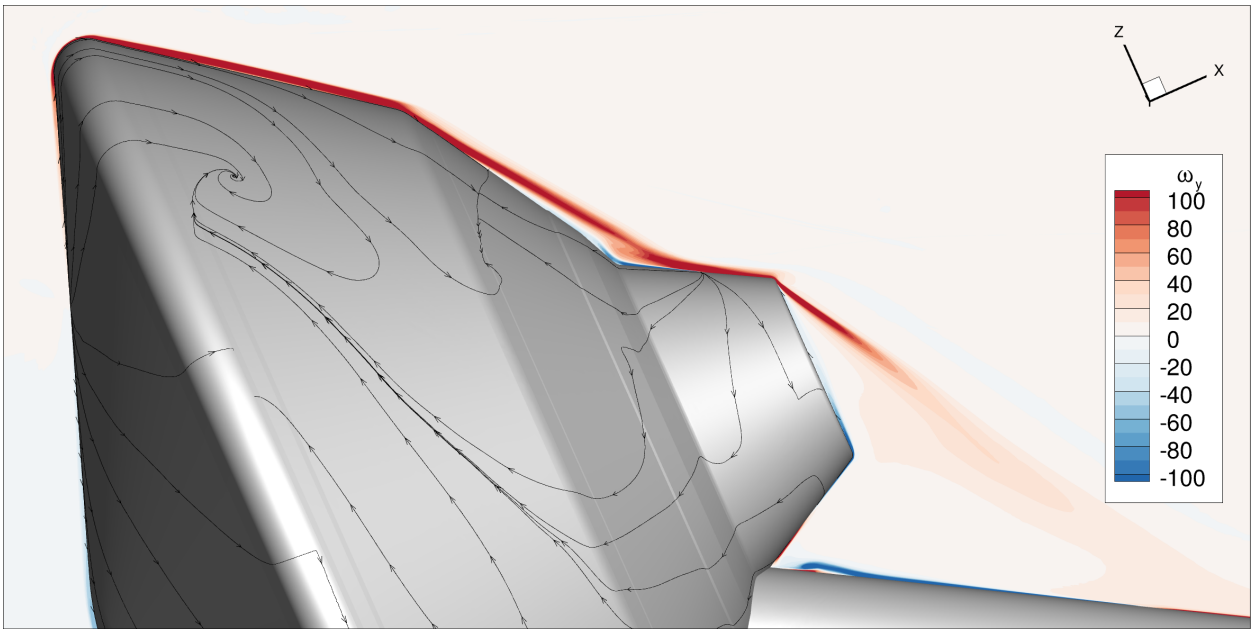

Fig. 22 A slice along the symmetry plane at $y = 0$, showing the vorticity in the y-direction, for Mach 2.5, $\alpha = -24°$. The vorticity is normalized by the vehicle diameter and the freestream velocity. The surface streamlines depict the skin friction. This case was run with the SST turbulence model.

pressures into agreement with the experimental data. The RC and QCR2000 model improvements have little effect on the pressure distribution across most of the vehicle. The compressibility correction in "SA-comp" increases the pressure across the base, as expected. This leads to a better prediction of overall drag. However, it does not remedy the unphysical variations in pressure across the base. For example, the original SA and SA-RC-QCR models predict a pressure at $z/D = 0$ that matches the experimental values, within the bounds of the experimental uncertainty. The compressibility correction predicts a higher pressure at this location, increasing the local errors. These difficulties with compressibility corrections match a study of an axisymmetric base flow by Forsythe et al. [7].

C. Mach 3.5

A smaller set of turbulence models were used for the Mach 3.5 and the Mach 4.5 cases. SA was the preference, since the SST model in FUN3D has received less attention and has several robustness issues. The predicted aerodynamic coefficients are plotted against the experimental data in Fig. 23. With the increased Mach number, the impact of backshell errors decreases. The axial force is still overpredicted at $\alpha = -16°$. Unlike at Mach 2.5, the predicted axial force at $\alpha = 0°$ is within the uncertainty bounds of the experimental data. However, this could be attributed to the larger experimental uncertainty at the higher Mach numbers. A closer look at the pressures for the $\alpha = -16°$ case can be seen in Fig. 24. As seen at Mach 2.5, the forebody pressures are predicted relatively accurately. The backshell pressures show a consistent underprediction, which is the reason for the overprediction in drag.

D. Mach 4.5

The predicted aerodynamic coefficients are plotted against the experimental data in Fig. 25. The CFD predictions of aerodynamic coefficients are in agreement with the experimental data, at least within the limits of the experimental uncertainty. Examining the surface pressures more closely reveals some modeling errors; a pressure profile for $\alpha = -16°$ case is shown in Fig. 26. The pressures along the forebody are overpredicted, which would increase predicted drag. Despite the consistent bias, the median relative error in c_p across all forebody taps, across all angles of attack is only 0.52%. These small errors are masked by a uniform underprediction of the pressure across the backshell. The backshell pressure tap data show that the turbulence model is still not accurately predicting the separated wake, despite relatively accurate predictions of the aerodynamic coefficients.

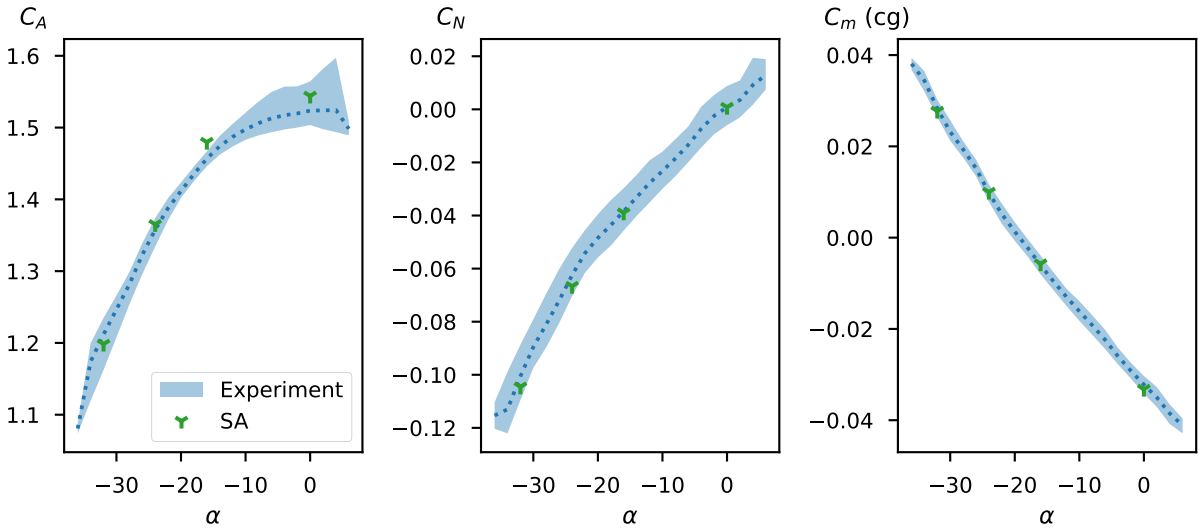

Fig. 23 Comparison of predicted aerodynamic coefficients with experimental data for the Mach 3.5 cases. The experimental data, with uncertainty, is indicated by the shaded regions.

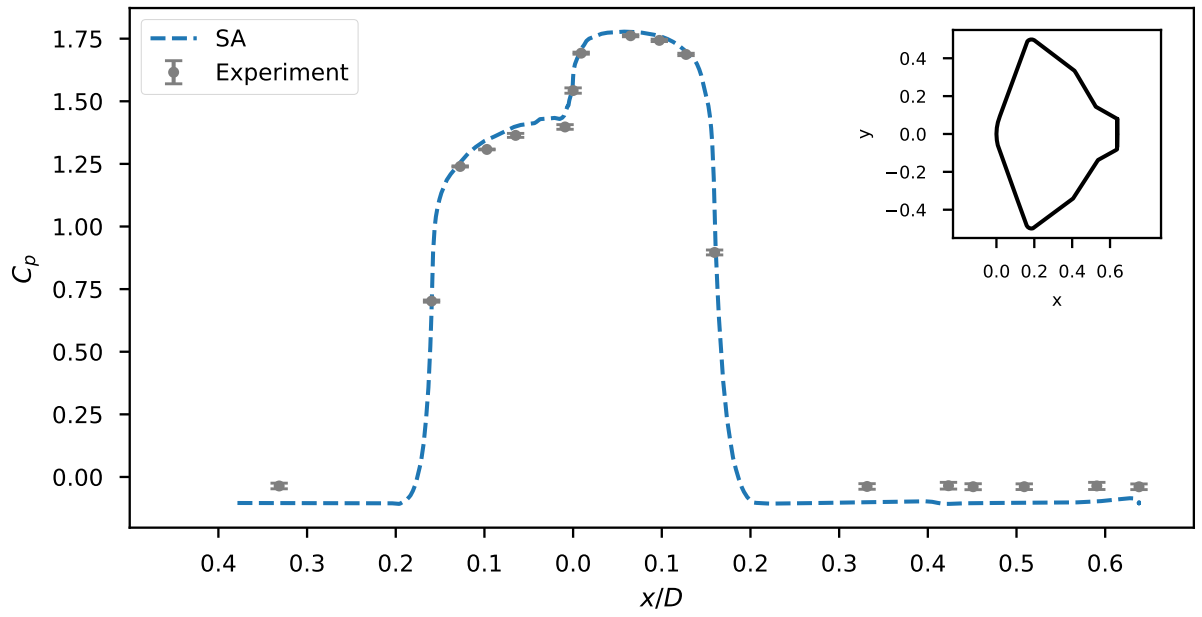

Fig. 24 Pressures along the symmetry plane, at Mach 3.5 and $\alpha = -16°$.

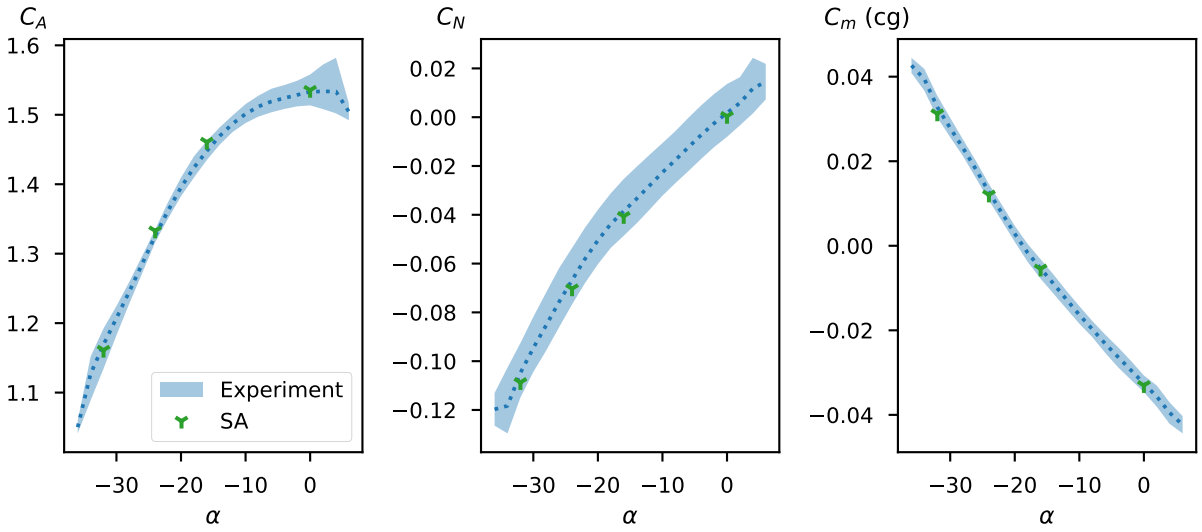

Fig. 25 Comparison of predicted aerodynamic coefficients with experimental data for the Mach 4.5 cases. The experimental data, with uncertainty, is indicated by the shaded regions.

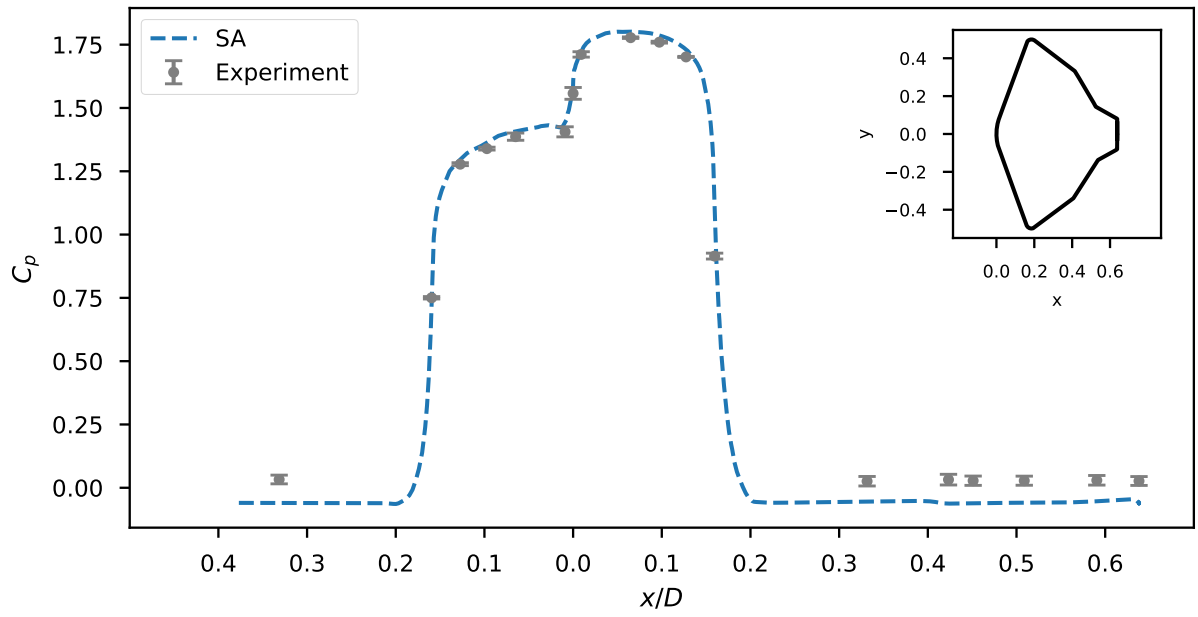

Fig. 26 Pressures along the symmetry plane, at Mach 4.5 and $\alpha = -16°$.

VI. Conclusions

The predictive accuracy of RANS models was evaluated on an MSL geometry. First, a forebody-only case was used to examine the sensitivity of aerodynamic coefficients to the grid. Several mesh generation techniques were evaluated. When comparing meshes with and without a frozen boundary layer, the differences between the predicted aerodynamic coefficients were small. Using a purely tetrahedral mesh with error-based mesh adaptation resulted in large wall-normal spacings, with a $\Delta y^+ \geq 10$. This is attributed to an imbalance between resolution of the bow shock and resolution of the boundary layer. However, using these large wall-normal spacings did not result in large changes to axial or normal forces when compared to meshes with prismatic boundary layers and tighter wall-normal spacings. This was believed to be due to the fact that pressure is dominated by inviscid effects from the exterior flow, with the viscous boundary layer having a secondary role.

Manually creating a prismatic boundary layer guarantees that the wall-normal spacing meets the common Δy^+ guidelines. However, the typical "frozen boundary layer" technique has a fixed amount of discretization error which does not go to zero as the exterior grid is refined. This results in different predictions for different frozen boundary layer grids. Ideally, the prismatic boundary layer should be refined along with the exterior grid.

There are several techniques that could be used to improve near-wall spacing with error-based mesh adaptation. The first is to use a manually-generated prismatic boundary-layer, with the caveat that the prismatic boundary must also be refined to obtain a grid-converged solution. Another option is to filter the scalar field prior to mesh adaptation; this will smooth out the solution around the shock, and limit the refinement there. A third suggestion is combining a scalar field that is more sensitive to boundary layers (such as density) with a scalar field that is more sensitive to shocks (such as pressure). This approach can be viewed as constructing a surrogate for an adjoint-based error estimator. More research is needed to explore these ideas and improve the reliability of error-based error adaptation for high-speed flows.

Next, the full vehicle was used to compare model predictions with steady RANS. The normal force and pitching moment matched the experimental values. As seen in previous studies by other authors, the axial force predicted using the Spalart Allmaras model at Mach 2.5. However, the SA-comp and SST models did predict lower drag than the baseline SA model, bringing the predictions within the experimental uncertainty bounds. Forebody pressures are also accurately predicted, and are relatively insensitive to the details of the turbulence model. Nevertheless, comparison of the surface pressure data shows a clear bias error, where all steady RANS models predicted backshell pressures lower than the experimental values. This is attributed to a known shortcoming of conventional RANS models, namely that the shear layer thickness is overpredicted for compressible wake flows. The predicted pressure also show unphysical variations across the backshell, which stand in contrast to the flatter, more uniform backshell pressure seen in experimental data. At Mach 3.5 and Mach 4.5, the underprediction of backshell pressure is still present. However, the backshell contribution to axial force is smaller, and the predicted axial force is more accurate.

When comparing the various options for turbulence models, the SST model gives more accurate predictions than SA for the integrated coefficients. The RC and QCR2000 improvements to the SA model did not significantly improve the predicted pressure across the backshell. Adding Spalart's compressibility correction [51] did result in higher pressure in the recirculation region and brought the aerodynamic coefficients into agreement with the experimental data. However, the correction did not improve the unphysical variations in predicted pressure across the backshell. In specific places, it made the predicted surface pressure *less* accurate.

While the axial force was predicted to within 1.6%, the results should be viewed cautiously. There are many differences between the wind tunnel experiments and flight, including the presence of a sting. Larger differences between RANS and CFD have been reported in other studies, such as Refs. [7, 8]. Hybrid RANS/LES may offer a more accurate prediction of pressure in separated wakes. Further research and development is needed for RANS and hybrid RANS/LES, so that improved accuracy can be obtained for multiple fidelity levels.

Acknowledgements

This work would not have been possible without Bil Kleb and Mike Park, who trailblazed the workflow used for the current paper. The authors also acknowledge the help of Kelly Murphy in explaining the experimental data. Much gratitude is owed to Kyle Thompson, Bil Kleb, Matt O'Connell for their comments and discussion on this paper. Gabriel Nastac and Jan-Renee Carlson also provided frequent feedback and discussions. Resources supporting this work were provided by the NASA High-End Computing (HEC) Program through the NASA Advanced Supercomputing (NAS) Division at Ames Research Center.

References

[1] Campbell, J. F., and Brown, C. A., "Experimental Wake Flow Properties of a Viking '75 Entry Vehicle," *Journal of Spacecraft and Rockets*, Vol. 11, No. 1, 1974, pp. 11–15. https://doi.org/10.2514/3.61997.

[2] Dyakonov, A., Schoenenberger, M., and Van Norman, J., "Hypersonic and Supersonic Static Aerodynamics of Mars Science Laboratory Entry Vehicle," *43rd AIAA Thermophysics Conference*, American Institute of Aeronautics and Astronautics, New Orleans, Louisiana, 2012. https://doi.org/10.2514/6.2012-2999.

[3] Karlgaard, C. D., Schoenenberger, M., Dutta, S., and Way, D. W., "Mars Entry, Descent, and Landing Instrumentation 2 Trajectory, Aerodynamics, and Atmosphere Reconstruction," *AIAA SCITECH 2022 Forum*, American Institute of Aeronautics and Astronautics, San Diego, CA & Virtual, 2022. https://doi.org/10.2514/6.2022-0423.

[4] Rodi, W., "Comparison of LES and RANS Calculations of the Flow around Bluff Bodies," *Journal of Wind Engineering and Industrial Aerodynamics*, Vol. 69–71, 1997, pp. 55–75. https://doi.org/10.1016/S0167-6105(97)00147-5.

[5] Iaccarino, G., Ooi, A., Durbin, P., and Behnia, M., "Reynolds Averaged Simulation of Unsteady Separated Flow," *International Journal of Heat and Fluid Flow*, Vol. 24, No. 2, 2003, pp. 147–156. https://doi.org/10.1016/S0142-727X(02)00210-2.

[6] Roy, C., Blottner, F., and Payne, J., "Bluff-Body Flow Simulations Using Hybrid RANS/LES," *33rd AIAA Fluid Dynamics Conference and Exhibit*, American Institute of Aeronautics and Astronautics, Orlando, Florida, 2003, pp. 1–11. https://doi.org/10.2514/6.2003-3889.

[7] Forsythe, J. R., Hoffmann, K. A., Cummings, R. M., and Squires, K. D., "Detached-Eddy Simulation With Compressibility Corrections Applied to a Supersonic Axisymmetric Base Flow," *Journal of Fluids Engineering*, Vol. 124, No. 4, 2002, pp. 911–923. https://doi.org/10.1115/1.1517572.

[8] Schwing, A. M., and Candler, G. V., "Detached-Eddy Simulation of Capsule Wake Flows and Comparison to Wind-Tunnel Test Data," *Journal of Spacecraft and Rockets*, Vol. 52, No. 2, 2015, pp. 439–449. https://doi.org/10.2514/1.A32834.

[9] Ekelschot, D., and Erb, A. J., "Studying the Effects of Anisotropic Mesh Adaptation with Comparison to MEDLI2 Flight Data," *Entry Systems Modeling Workshop*, NASA Kennedy Space Center, 2022.

[10] Brandis, A. M., White, T. R., Saunders, D. A., Hill, J. P., and Johnston, C. O., "Simulation of the Schiaparelli Entry and Comparison to Aerosciences Flight Data," *Journal of Spacecraft and Rockets*, Vol. 59, No. 1, 2022, pp. 166–177. https://doi.org/10.2514/1.A35049.

[11] Mitcheltree, R. A., "Corrections to Drag Coefficient Due to Base Pressure," Internal Memo, NASA Langley Research Center, Hampton, VA, 1995.

[12] Dutta, S., Karlgaard, C. D., Kass, D., Villar, G., and Mischna, M., "Post-Flight Analysis of Atmospheric Properties from Mars 2020 Entry, Descent, and Landing," *AIAA SCITECH 2022 Forum*, American Institute of Aeronautics and Astronautics, San Diego, CA & Virtual, 2022, pp. 1–19. https://doi.org/10.2514/6.2022-0422.

[13] Polsgrove, T., Percy, T. K., Sutherlin, S., Dwyer-Cianciolo, A. M., Dillman, R., Brune, A., Cassell, A., and Johnston, C., "Human Mars Entry, Descent, and Landing Architecture Study: Deployable Decelerators," *2018 AIAA SPACE and Astronautics Forum and Exposition*, American Institute of Aeronautics and Astronautics, Orlando, FL, 2018, pp. 1–16. https://doi.org/10.2514/6.2018-5191.

[14] Schoenenberger, M., Brown, T. G., and Yates, L., "Surface Pressure Ballistic Range Test of Mars 2020 Capsule in Support of MEDLI2," *35th AIAA Applied Aerodynamics Conference*, American Institute of Aeronautics and Astronautics, Denver, Colorado, 2017, pp. 1–26. https://doi.org/10.2514/6.2017-4079.

[15] Barnhardt, M., Candler, G., and MacLean, M., "CFD Analysis of CUBRC Base Flow Experiments," *48th AIAA Aerospace Sciences Meeting Including the New Horizons Forum and Aerospace Exposition*, American Institute of Aeronautics and Astronautics, Orlando, Florida, 2010. https://doi.org/10.2514/6.2010-1250.

[16] Slotnick, J., Khodadoust, A., Alonso, J., Darmofal, D., Gropp, W., Lurie, E., and Mavriplis, D., "CFD Vision 2030 Study: A Path to Revolutionary Computational Aerosciences," NASA CR 2014-218178, NASA Langley Research Center, Hampton, VA, Mar. 2014.

[17] Spalart, P. R., Jou, W., Strelets, M., and Allmaras, S. R., "Comments on the Feasibility of LES for Wings, and on a Hybrid RANS/LES Approach," *Advances in DNS/LES, 1st AFOSR Int Conf*, Columbus, OH, 1997.

[18] Forsythe, J. R., Squires, K. D., Wurtzler, K. E., and Spalart, P. R., "Detached-Eddy Simulation of the F-15E at High Alpha," *Journal of Aircraft*, Vol. 41, No. 2, 2004, pp. 193–200. https://doi.org/10.2514/1.2111.

[19] Thompson, K. B., Wise, A. J., Hollis, B. R., and Hinkle, A. D., "Improvements to the LAURA Mesh Adaptation Algorithm," *AIAA AVIATION 2023 FORUM*, American Institute of Aeronautics and Astronautics, San Diego, CA, 2023.

[20] Schoenenberger, M., Cheatwood, F. M., and Desai, P., "Static Aerodynamics of the Mars Exploration Rover Entry Capsule," *43rd AIAA Aerospace Sciences Meeting and Exhibit*, American Institute of Aeronautics and Astronautics, Reno, Nevada, 2005, pp. 1–12. https://doi.org/10.2514/6.2005-56.

[21] Prince, J. L., and Shoenenberger, M., "Independent Assessment of the Backshell Pressure Field for Mars Entry, Descent, and Landing Instrumentation 2 (MEDLI2)," NASA TM 2017-219666, NASA Langley Research Center, Hampton, VA, 2017.

[22] Kleb, W. L., Schoenenberger, M., Korzun, A. M., and Park, M. A., "Sketch-to-Solution: A Case Study in RCS Aerodynamic Interaction," *AIAA Scitech 2020 Forum*, American Institute of Aeronautics and Astronautics, Orlando, FL, 2020. https://doi.org/10.2514/6.2020-0673.

[23] Ekelschot, D., and Brock, J., "Enabling Metric-Based Mesh Adaptation for Advanced Compressible Flow Simulations Using US3D," *AIAA SCITECH 2022 Forum*, American Institute of Aeronautics and Astronautics, San Diego, CA, 2022, pp. 1–18. https://doi.org/10.2514/6.2022-1866.

[24] Ekelschot, D., and Brock, J. M., "Effect of Anisotropic Mesh Adaptation on Surface Pressure Predictions for Atmospheric Entry Simulations." *11th International Conference on Computational Fluid Dynamics*, Maui, HI, 2022, pp. 1–13.

[25] Nakahashi, K., "Viscous Flow Computations Using a Composite Grid," *8th Computational Fluid Dynamics Conference*, American Institute of Aeronautics and Astronautics, Honolulu,HI,U.S.A., 1987. https://doi.org/10.2514/6.1987-1128.

[26] Kallinderis, Y., and Ward, S., "Prismatic Grid Generation with an Efficient Algebraic Method for Aircraft Configurations," *10th Applied Aerodynamics Conference*, American Institute of Aeronautics and Astronautics, Palo Alto,CA,U.S.A., 1992. https://doi.org/10.2514/6.1992-2721.

[27] Kallinderis, Y., Khawaja, A., and McMorris, H., "Hybrid Prismatic/Tetrahedral Grid Generation for Viscous Flows around Complex Geometries," *AIAA Journal*, Vol. 34, No. 2, 1996, pp. 291–298. https://doi.org/10.2514/3.13063.

[28] McCloud, P. L., "Best Practices for Unstructured Grid Shock Fitting," *55th AIAA Aerospace Sciences Meeting*, American Institute of Aeronautics and Astronautics, Grapevine, Texas, 2017, pp. 1–14. https://doi.org/10.2514/6.2017-1149.

[29] Nastac, G., Tramel, R. W., and Nielsen, E. J., "Improved Heat Transfer Prediction for High-Speed Flows over Blunt Bodies Using Adaptive Mixed-Element Unstructured Grids," *AIAA SCITECH 2022 Forum*, American Institute of Aeronautics and Astronautics, San Diego, CA & Virtual, 2022, pp. 1–26. https://doi.org/10.2514/6.2022-0111.

[30] Roe, P. L., "Error Estimates for Cell-Vertex Solutions of the Compressible Euler Equations," NASA CR 178235, NASA Langley Research Center, Hampton, VA, Jan. 1987.

[31] Nishikawa, H., "On the Loss and Recovery of Second-Order Accuracy with U-MUSCL," *Journal of Computational Physics*, Vol. 417, 2020, p. 109600. https://doi.org/10.1016/j.jcp.2020.109600.

[32] Nishikawa, H., "Two Ways to Extend Diffusion Schemes to Navier-Stokes Schemes: Gradient Formula or Upwind Flux," *20th AIAA Computational Fluid Dynamics Conference*, American Institute of Aeronautics and Astronautics, Honolulu, Hawaii, 2011. https://doi.org/10.2514/6.2011-3044.

[33] Brown, J., "Turbulence Model Validation for Hypersonic Flows," *8th AIAA/ASME Joint Thermophysics and Heat Transfer Conference*, American Institute of Aeronautics and Astronautics, St. Louis, Missouri, 2002, pp. 1–22. https://doi.org/10.2514/6.2002-3308.

[34] Schoenenberger, M., Dyakonov, A., Buning, P., Scallion, B., and Van Norman, J., "Aerodynamic Challenges for the Mars Science Laboratory Entry Descent and Landing," *41st AIAA Thermophysics Conference*, American Institute of Aeronautics and Astronautics, San Antonio, Texas, 2009, pp. 1–29. https://doi.org/10.2514/6.2009-3914.

[35] Settles, G. S., and Dodson, L. J., "Supersonic and Hypersonic Shock/Boundary-Layer Interaction Database," *AIAA Journal*, Vol. 32, No. 7, 1994, pp. 1377–1383. https://doi.org/10.2514/3.12205.

[36] Ross, J. C., Heineck, J. T., Burnside, N., Sellers, M. E., Halcomb, N., Garbeff, T., Yamauchi, G., and Kushner, L., "Comprehensive Study of the Flow Around a Simplified Orion Capsule Model," *31st AIAA Applied Aerodynamics Conference*, American Institute of Aeronautics and Astronautics, San Diego, CA, 2013. https://doi.org/10.2514/6.2013-2815.

[37] Anderson, W. K., Biedron, R. T., Carlson, J.-R., Derlaga, J. M., Druyor, C. T., Gnoffo, P. A., Hammond, D. P., Jacobson, K. E., Jones, W. T., Kleb, W., Lee-Rausch, E. M., Nastac, G., Nielsen, E. J., Park, M. A., Rumsey, C. L., Thomas, J. L., Thompson, K. B., Walden, A., Wang, L., Wood, S. L., Wood, W. A., Diskin, B., Liu, Y., and Zhang, X., "FUN3D Manual: 14.0," NASA TM 20220017743, NASA Langley Research Center, Hampton, VA, Dec. 2022.

[38] Liu, Y., and Nishikawa, H., "Third-Order Inviscid and Second-Order Hyperbolic Navier-Stokes Solvers for Three-Dimensional Unsteady Inviscid and Viscous Flows," *55th AIAA Aerospace Sciences Meeting*, American Institute of Aeronautics and Astronautics, Grapevine, Texas, 2017. https://doi.org/10.2514/6.2017-0738.

[39] Carlson, J.-R., "Inflow/Outflow Boundary Conditions with Application to FUN3D," NASA TM–2011-217181, NASA Langley Research Center, Hampton, VA, Oct. 2011.

[40] Candler, G., Barnhardt, M., Drayna, T., Nompelis, I., Peterson, D., and Subbareddy, P., "Unstructured Grid Approaches for Accurate Aeroheating Simulations," *18th AIAA Computational Fluid Dynamics Conference*, American Institute of Aeronautics and Astronautics, Miami, Florida, 2007. https://doi.org/10.2514/6.2007-3959.

[41] Bardina, J. E., Huang, P. G., and Coakley, T. J., "Turbulence Modeling Validation, Testing, and Development," NASA TM-110446, NASA Langley Research Center, Hampton, VA, Apr. 1997.

[42] Kleb, W. L., Park, M. A., Wood, W. A., Bibb, K. L., Thompson, K. B., and Gomez, R. J., "Sketch-to-Solution: An Exploration of Viscous CFD with Automatic Grids," *AIAA Aviation 2019 Forum*, American Institute of Aeronautics and Astronautics, Dallas, Texas, 2019. https://doi.org/10.2514/6.2019-2948.

[43] Park, M. A., and DeSpirito, J., "The Influence of Adaptive Mesh Refinement on the Prediction of Vortex Interactions about a Generic Missile Airframe," *AIAA SCITECH 2022 Forum*, American Institute of Aeronautics and Astronautics, San Diego, CA & Virtual, 2022. https://doi.org/10.2514/6.2022-1177.

[44] Alauzet, F., and Loseille, A., "High-Order Sonic Boom Modeling Based on Adaptive Methods," *Journal of Computational Physics*, Vol. 229, No. 3, 2010, pp. 561–593. https://doi.org/10.1016/j.jcp.2009.09.020.

[45] Loseille, A., and Alauzet, F., "Continuous Mesh Framework Part I: Well-Posed Continuous Interpolation Error," *SIAM Journal on Numerical Analysis*, Vol. 49, No. 1, 2011, pp. 38–60. https://doi.org/10.1137/090754078.

[46] Loseille, A., and Alauzet, F., "Continuous Mesh Framework Part II: Validations and Applications," *SIAM Journal on Numerical Analysis*, Vol. 49, No. 1, 2011, pp. 61–86. https://doi.org/10.1137/10078654X.

[47] Park, M., and Carlson, J.-R., "Turbulent Output-Based Anisotropic Adaptation," *48th AIAA Aerospace Sciences Meeting Including the New Horizons Forum and Aerospace Exposition*, American Institute of Aeronautics and Astronautics, Orlando, Florida, 2010. https://doi.org/10.2514/6.2010-168.

[48] Allmaras, S. R., Johnson, F. T., and Spalart, P. R., "Modifcations and Clarifcations for the Implementation of the Spalart-Allmaras Turbulence Model," *Computational Fluid Dynamics*, 2012, pp. 1–11.

[49] Shur, M. L., Strelets, M. K., Travin, A. K., and Spalart, P. R., "Turbulence Modeling in Rotating and Curved Channels: Assessing the Spalart-Shur Correction," *AIAA Journal*, Vol. 38, No. 5, 2000, pp. 784–792. https://doi.org/10.2514/2.1058.

[50] Spalart, P. R., "Strategies for Turbulence Modelling and Simulations," *International Journal of Heat and Fluid Flow*, Vol. 21, No. 3, 2000, pp. 252–263.

[51] Spalart, P., "Trends in Turbulence Treatments," *Fluids 2000 Conference and Exhibit*, AIAA, Denver, CO, 2000. https://doi.org/10.2514/6.2000-2306.

[52] Menter, F. R., "Two-Equation Eddy-Viscosity Turbulence Models for Engineering Applications," *AIAA Journal*, Vol. 32, No. 8, 1994, pp. 1598–1605. https://doi.org/10.2514/3.12149.

[53] Roache, P. J., "Perspective: A Method for Uniform Reporting of Grid Refinement Studies," *Journal of Fluids Engineering*, Vol. 116, No. 3, 1994, pp. 405–413. https://doi.org/10.1115/1.2910291.

[54] Roache, P. J., "Verification of Codes and Calculations," *AIAA Journal*, Vol. 36, No. 5, 1998, pp. 696–702. https://doi.org/10.2514/2.457.